CANCER

Epigenetically heterogeneous tumor cells direct collective invasion through filopodia-driven fibronectin micropatterning

Emily R. Summerbell[1]*, Janna K. Mouw[2,3]*, Joshua S. K. Bell[4]†, Christina M. Knippler[2,3],
Brian Pedro[1], Jamie L. Arnst[2,3], Tala O. Khatib[5], Rachel Commander[1], Benjamin G. Barwick[2,3],
Jessica Konen[1]‡, Bhakti Dwivedi[3], Sandra Seby[3], Jeanne Kowalski[3,6]§,
Paula M. Vertino[3,7||¶], Adam I. Marcus[2,3]#

Tumor heterogeneity drives disease progression, treatment resistance, and patient relapse, yet remains largely underexplored in invasion and metastasis. Here, we investigated heterogeneity within collective cancer invasion by integrating DNA methylation and gene expression analysis in rare purified lung cancer leader and follower cells. Our results showed global DNA methylation rewiring in leader cells and revealed the filopodial motor *MYO10* as a critical gene at the intersection of epigenetic heterogeneity and three-dimensional (3D) collective invasion. We further identified JAG1 signaling as a previously unknown upstream activator of *MYO10* expression in leader cells. Using live-cell imaging, we found that MYO10 drives filopodial persistence necessary for micropatterning extracellular fibronectin into linear tracks at the edge of 3D collective invasion exclusively in leaders. Our data fit a model where epigenetic heterogeneity and JAG1 signaling jointly drive collective cancer invasion through MYO10 up-regulation in epigenetically permissive leader cells, which induces filopodia dynamics necessary for linearized fibronectin micropatterning.

INTRODUCTION

Tumor heterogeneity drives disease progression and treatment resistance, yet most cancer research and therapy decisions are carried out at the whole-population level (*1*, *2*). The polyclonal nature of metastatic lesions suggests that they originate from heterogeneous clusters of collectively invading cells, rather than clonally from singular disseminated cells (*3–5*). During the initial steps of tumor invasion, many solid tumors of epithelial origin rely on collective invasion, in which packs of cells invade into the adjacent stroma while maintaining cell-cell contacts (*6*, *7*). Collective invasion packs correlate with higher histologic tumor grade and increased metastatic potential, demonstrating the importance of understanding how intratumor heterogeneity propagates invasion and metastasis (*7–9*). Nevertheless, the molecular mechanisms underlying the formation and function of heterogeneous collective invasion packs remain poorly understood.

Heterogeneous collective invasion packs can contain phenotypically distinct invasive "leader" and noninvasive "follower" cell populations (*6*, *10–13*). Although the specific markers of leader and follower cells may vary based on the tissue of origin, effective cooperation between leader and follower subpopulations invariably promotes the survival and invasion of collectively invading cancer cells (*6*, *10*). Cooperation between leader and follower cells frequently necessitates hijacking developmental cell-cell signaling pathways, including the Notch pathway and vascular endothelial growth factor–dependent noncanonical angiogenic mimicry (*14*). Despite a growing understanding of the underlying genetic and transcriptomic differences between tumor subpopulations, little is known about the epigenetic factors that underlie heterogeneous phenotype determination and plasticity within the collective invasion pack.

We sought to use epigenetic heterogeneity to identify key regulators of phenotypic heterogeneity, cell-cell cooperation, and collective tumor invasion. To do this, we integrated DNA methylation array data with RNA sequencing (RNA-seq) expression data on purified populations of lung cancer leader and follower cells. We found vast rewiring of the DNA methylome and transcriptome unique to leader cells compared with follower cells or the parental population, including substantial enrichment for differential DNA methylation and gene expression across several pathways that fundamentally regulate multicellular collective invasion. Integration of DNA methylation and transcriptome data identified the filopodia protein myosin-X (*MYO10*) at the intersection of epigenetic regulation and collective cancer cell invasion in leader cells. Filopodia are thin finger-like membrane protrusions at the periphery of cells that critically support cell adhesion, migration, invasion, and extracellular mechanosensing in both normal physiology and in cancer (*15*). As a motor protein that localizes to filopodia tips, MYO10 drives filopodial maintenance and function by transporting key cargo to filopodia tips, including integrins and actin anticapping proteins (*16–18*). Since *MYO10* was binarily expressed only in our leader cells, we sought to determine whether MYO10 serves a previously unrecognized leader cell–specific role within filopodia during collective invasion. In

[1]Graduate Program in Cancer Biology, Emory University, Atlanta, GA, USA. [2]Department of Hematology and Medical Oncology, Emory University, Atlanta, GA, USA. [3]Winship Cancer Institute, Emory University, Atlanta, GA, USA. [4]Graduate Program in Genetics and Molecular Biology, Emory University, Atlanta, GA, USA. [5]Graduate Program in Biochemistry, Cell and Developmental Biology, Emory University, Atlanta, GA, USA. [6]Department of Biostatistics and Bioinformatics, Emory University, Atlanta, GA, USA. [7]Department of Radiation Oncology, Emory University, Atlanta, GA, USA.
*These authors contributed equally to this work.
†Present address: Tempus Labs Inc., Chicago, IL, USA.
‡Present address: Department of Thoracic/Head and Neck Medical Oncology, University of Texas MD Anderson Cancer Center, Houston, TX, USA.
§Present address: Department of Oncology, The University of Texas at Austin, Dell Medical School, Austin, TX, USA.
||Present address: Department of Biomedical Genetics, University of Rochester School of Medicine and Dentistry, Rochester, NY, USA.
¶Present address: Wilmot Cancer Institute, Rochester, NY, USA.
#Corresponding author. Email: aimarcu@emory.edu

summary, we demonstrate that lung cancer collective invasion is facilitated by DNA methylation heterogeneity and JAG1 activity that jointly drive MYO10 overexpression and localization to the tips of filopodia within specialized leader cells, which allows stable leader cell filopodia to actively guide linear fibronectin micropatterning and induce three-dimensional (3D) collective cell invasion.

RESULTS
Epigenetic heterogeneity between lung cancer leader cells and follower cells reveals functionally relevant determinants of phenotype heterogeneity

We purified leader and follower cell subpopulations from invading spheroids of the H1299 lung cancer cell line using SaGA (10). To explore the epigenetic differences that underlie leader and follower behavior, we performed an Illumina Infinium MethylationEPIC 850K DNA methylation microarray on purified leader and follower cells and on the parental population from which these cells were derived. The 5000 most variant CpG sites (i.e., differentially methylated cytosine-guanine dinucleotide probes, or DMPs) were independently clustered by cell type (Fig. 1A). Leader cells displayed a significant shift toward hypermethylation across all CpG sites, with a 10% increase in the genome-wide median beta value compared to follower and parental cells (fig. S1, A and B).

We identified 3322 differentially methylated regions (DMRs) with a beta value difference $\geq$ 0.2 between two of the three populations (Fig. 1B). While only one DMR was differentially methylated in follower cells compared to parental cells, 3308 DMRs were differentially methylated in leader cells compared to follower cells and/or the parental population, and 13 DMRs differed between all three groups (with all 13 showing mean beta values in the order of followers < parental < leaders). In addition, 79% of the 3308 DMRs were hypermethylated in leader cells compared to follower and/or parental cells, while the remaining 21% were hypomethylated in leader cells (fig. S1C). DMPs between leader and follower cells were enriched for noncoding regulatory elements and intergenic regions and were less frequent in proximal promoters and intragenic regions (Fig. 1C). Overall, our data showed that DNA methylation within follower cells and parental cells was similar, but leader cells expressed unique patterns of DNA methylation compared to follower or parental cells.

We next performed RNA-seq on isolated leader and follower cells and the parental population to assess gene expression differences (13). Principal component analysis showed that parental, leader, and follower cells each had distinct gene expression patterns (fig. S1D). To identify the subset of genes that was the most differentially expressed between each phenotype, we identified the 98th percentile most variant genes (499 genes) between all three cell types (Fig. 1D). Within the top 15 most differentially expressed genes, myosin-X (MYO10), fibronectin (FN1), and the Notch ligand Jagged-1 (JAG1) were highly expressed in leader cells compared to follower cells (Fig. 1E). Among the differentially expressed genes were regulators of DNA cytosine methylation, with leader cells expressing a distinctive pattern of these genes compared to follower and parental cells (fig. S1E).

Since DNA methylation at CpG islands (CGIs) within gene promoters negatively regulates gene expression (19, 20), we identified 123 genes that exhibited both a significant difference in gene expression (twofold normalized gene count difference and adjusted $P < 0.01$) and differentially methylated CGIs overlapping the proximal promoter when comparing leader cells and follower cells (Fig. 1F).

Of the genes identified, 72 exhibited hypermethylation of the promoter and were underexpressed in leader cells relative to followers, whereas 13 showed the opposite relationship (e.g., a hypomethylated promoter and overexpressed in leaders compared to follower cells), consistent with the well-described negative correlation between promoter methylation and gene expression (Fig. 1F) (19, 20). When we looked beyond the promoter and searched for DMRs that overlap any portion of expressed genes, we identified 905 DMRs that overlap the promoter and/or gene body of differentially expressed genes (fig. S1F). Gene set enrichment analysis (GSEA) of genes differentially expressed between leaders and followers independent of DNA methylation aligned with previous transcriptome analysis by microarray (10) and emphasized many pathways critical for collective migration in cancer, angiogenesis, and axon guidance (fig. S2) (4, 21–24). However, GSEA of differentially methylated genes between leaders and followers revealed that only leader cells but not followers contained gene sets that were differentially methylated (fig. S1G). The combined GSEA analyses in leader cells compared to follower cells overlapped at several key pathways relevant to collective migration in both cancer and normal physiology, such as Notch1 signaling, axon guidance, angiogenesis, and extracellular matrix (ECM)–receptor interactions (fig. S1G). These data demonstrate considerable heterogeneity across both DNA methylation and gene expression between leader cells and follower cells that overlaps with many biologically relevant pathways, recapitulating intratumor heterogeneity observed in primary patient samples.

Myosin-X is enriched in leader cells
From our integrated DNA methylation and gene expression analysis, we identified MYO10 as the gene most significantly up-regulated and hypomethylated at the promoter in leader cells compared to follower cells (Fig. 1F). MYO10 is an unconventional myosin that localizes to filopodia tips and drives filopodia elongation (16, 25). Annotation of the MYO10 DMPs revealed that CpG probes within 1500 bp of the promoter and the first exon were hypomethylated in leader cells compared to follower cells, whereas almost all CpG probes within the gene body were hypermethylated compared to follower cells (Fig. 1G and fig. S3A). Because promoter methylation acts as a transcriptional repressor (19, 20) and gene body methylation positively correlates with gene expression (26), these data suggest that shifts in MYO10 DNA methylation may enable MYO10 overexpression in leader cells. Overexpression of MYO10 in leader cells observed by RNA-seq was validated by quantitative polymerase chain reaction (qPCR) and western blot (Fig. 1, H and I). Leader cells expressed endogenous MYO10 within filopodia in 2D cell culture (Fig. 1J) and the non–small-cell lung carcinoma (NSCLC) parental cell lines H1299, H1792, and H1975 (Fig. 1K). During 3D spheroid collective invasion, leader cells were enriched for MYO10 compared to follower cells (Fig. 1L). Collectively invading spheroids of the parental H1299, H1792, and H1975 cell lines also showed enriched MYO10 expression in cells at the front of invasive chains compared to cells further back in these collective chains (Fig. 1M). These data suggest MYO10 is highly expressed in invasive NSCLC leader cells but not follower cells.

MYO10 regulates filopodia length, cell motility, and collective invasion
Since filopodia regulate many aspects of cancer cell adhesion and invasion (15), we wanted to determine whether MYO10-driven filopodia
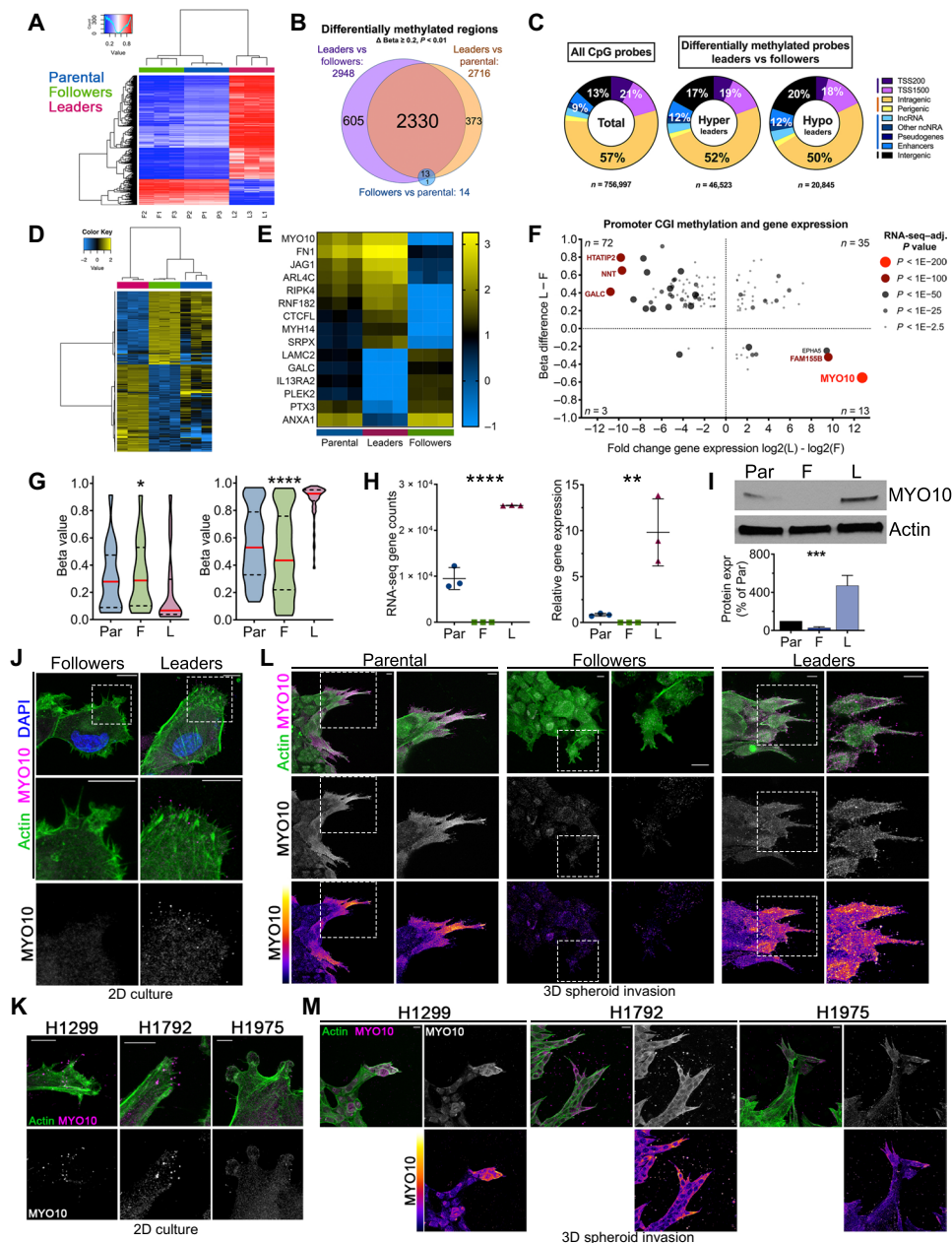
Fig. 1. DNA methylation heterogeneity reveals that MYO10 is differentially methylated and overexpressed in leader cells. (**A**) Heat map of MethylationEPIC array beta values for the 5000 most differentially methylated CpG probes (DMPs). (**B**) Venn diagram of differentially methylated regions (DMRs) with a beta difference ≥ 0.2 and adjusted $P < 0.01$. (**C**) Annotation of DMPs across genomic features. (**D** and **E**) Heat maps, z scores from log 2–normalized RNA-seq expression counts of most differentially expressed (DE) genes. (D) 98th percentile genes ($N = 499$) scaled by row and column. (E) Subset of the 15 most DE genes, without clustering. (**F**) Scatter plot of promoter CpG island (CGI) methylation beta differences and RNA-seq log 2 fold changes for all genes that are both differentially expressed (≥twofold difference, $P < 0.01$) and differentially methylated at the CGI (≥0.2 difference) between leaders and followers. (**G**) Violin plots of beta values for CpGs within the MYO10 TS1500 promoter ($N = 18$ probes) or MYO10 gene body ($N = 95$ probes). Kruskal-Wallis test with Dunn's correction. (**H**) MYO10 expression by RNA-seq (left) or quantitative polymerase chain reaction (qPCR; right). Ordinary one-way analysis of variance (ANOVA) with Tukey's correction. (**I**) Western blot, MYO10, actin as loading control. $n = 5$. (**J** and **K**) MYO10 immunofluorescence, follower and leader cells (J) or H1299, H1792, and H1975 NSCLC cells (K). Scale bars, 5 μm; representative images from $n = 3$, $N ≥ 30$ cells per cell type. (**L** and **M**) MYO10 immunofluorescence, 3D spheroid invasion of H1299 parental, follower, and leader cells (L) or of H1299, H1792, and H1975 NSCLC cells (M). Fire lookup table represents MYO10 signal intensity. Scale bars, 10 μm. (A to M) Unless noted, $n = 3$. Par, parental; F, followers. $*P < 0.05$, $**P < 0.01$, $***P < 0.001$, and $****P < 0.0001$.

functionally regulate leader cell migration and invasion. We quantified filopodia length in leaders and followers during 3D collective invasion (Fig. 2A). Follower cells almost exclusively displayed short filopodia (mean length, 1.5 μm) compared to leader cell filopodia (mean length, 3.4 μm). To determine how the MYO10 expression affects leader cell filopodial dynamics, we depleted *MYO10* via small interfering RNA (siRNA) in leader cells (fig. S3B), which resulted in considerably shorter filopodia (mean length, 1.5 μm) reminiscent
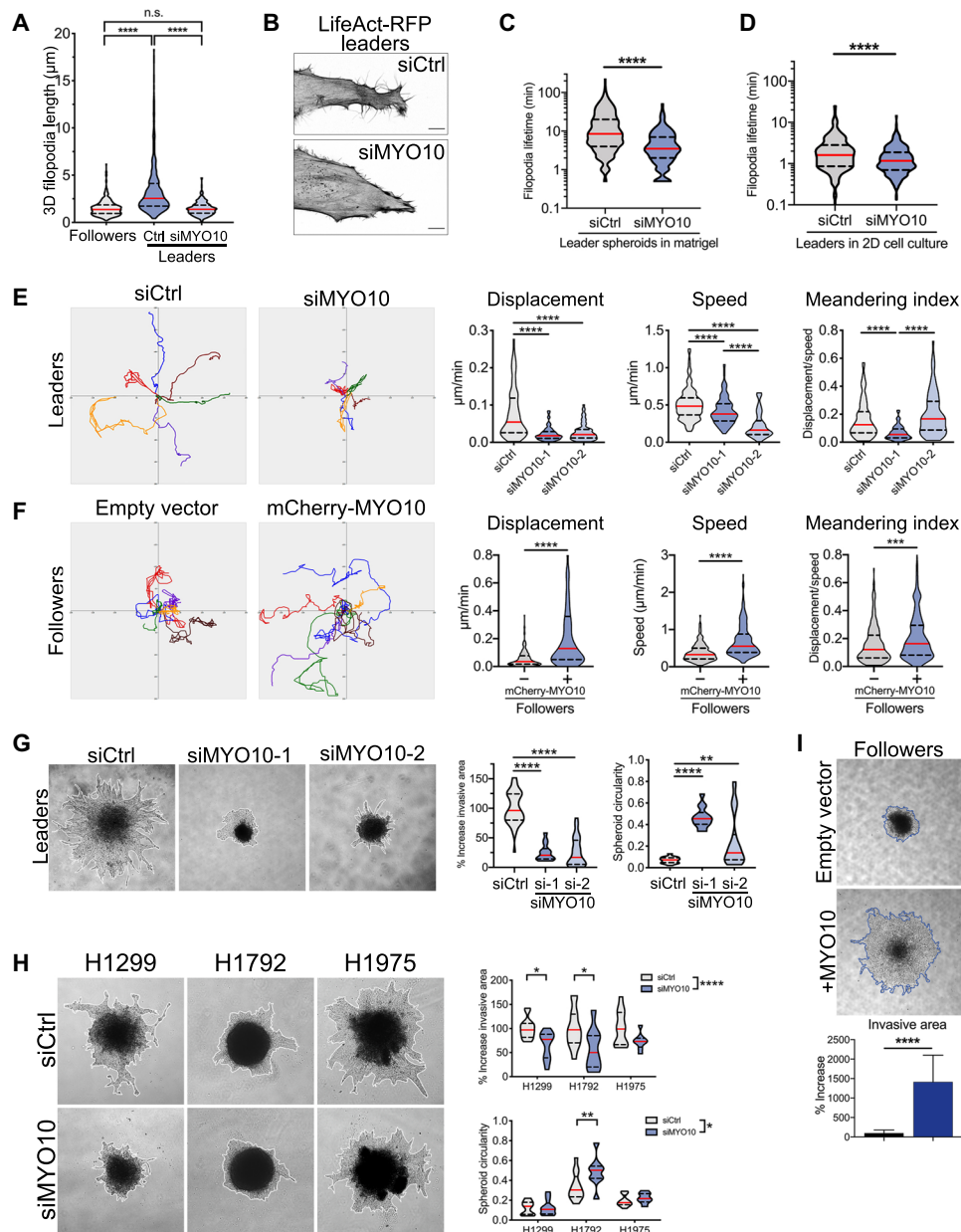
Fig. 2. MYO10 regulates cell motility and collective invasion. (**A**) Violin plot of filopodia lengths during 3D invasion of followers, si-control (siCtrl) leaders, and siMYO10 leaders. Red line, median, dashed black lines, interquartile range. Kruskal-Wallis test with Dunn's correction for multiple comparisons. n.s., not significant. (**B**) Representative images from live-cell imaging of LifeAct-RFP filopodia dynamics in leaders expressing siCtrl or siMYO10. Scale bars, 10 μm. (**C**) Violin plot of filopodia lifetimes during 3D spheroid invasion of siCtrl leaders and siMYO10 leaders. Kruskal-Wallis test with Dunn's correction for multiple comparisons. (**D**) Violin plot of filopodia lifetimes in 2D of siCtrl leaders and siMYO10 leaders. Kruskal-Wallis test with Dunn's correction for multiple comparisons. (**E** and **F**) Live-cell tracking analysis of 2D cell migration of leaders expressing siCtrl or siMYO10 (E) or in followers expressing a control mCherry vector or mCherry-MYO10 (F). (**G**) Representative images and quantification of 72-hour spheroid invasion assays H1299 leaders expressing siCtrl or one of two MYO10 siRNAs (siMYO10-1 and siMYO10-2). Kruskal-Wallis test with Dunn's correction for multiple comparisons. (**H**) Representative images and quantification of 72-hour spheroid invasion assays of parental H1299, H1792, and H1975 cells expressing siCtrl one of two MYO10 siRNAs (siMYO10-1 and siMYO10-2). Two-way ANOVA with Sidak's multiple comparison test. Effect of the siRNA indicated to the right of the key. Representative images and quantification of 48-hour invasion assays in Matrigel of follower cells expressing a control empty vector or mCherry-MYO10. Mann-Whitney U test, two-tailed. For all panels: unless noted, $n = 3$; *$P < 0.05$, **$P < 0.01$, ***$P < 0.001$, and ****$P < 0.0001$.

of filopodia observed in follower cells and consistent with previous work demonstrating MYO10-driven filopodia elongation on 2D substrates (Fig. 2, A to C, and movies S1 and S2) (*27–29*). When we assessed filopodia lifetimes in our si-control (siCtrl) versus siMYO10

leader cells during 3D invasion, we observed prolonged filopodial lifetimes compared to filopodial lifetimes reported in 2D (Fig. 2, C and D) (*27–29*), confirming significantly different filopodia dynamics in 3D versus 2D for our leader cell subpopulation.

To determine how MYO10 affected 2D cell motility and 3D invasion, we modulated *MYO10* expression in both leader and follower cell subpopulations (fig. S3, B and C). *MYO10* knockdown in leader cells greatly decreased cell motility in 2D, while *MYO10* overexpression in follower cells increased cell motility (Fig. 2, E and F). *MYO10* knockdown in leader cells and in three parental NSCLC cell lines abrogated chain-like collective invasion (Fig. 2, G and H). Conversely, ectopic mCherry-*MYO10* expression in follower cells induced long filopodia and markedly increased 3D spheroid invasion (Fig. 2I). These data suggest that MYO10 is necessary for collective invasion via its role in leader cell filopodia.

JAG1 expression is elevated in leader cells
The absence of *MYO10* promoter methylation in leader cells relative to followers is indicative of a more permissive chromatin environment but, in itself, is not deterministic of gene expression levels. Given the abundant up-regulation of *MYO10* in leaders, we therefore examined our transcriptome analysis for putative pathways that might impinge upon the locus to regulate *MYO10* expression. The Notch signaling pathway is an evolutionarily conserved pathway composed of four Notch receptors (Notch1 to Notch4) and five canonical ligands (JAG1, JAG2, DLL1, DLL3, and DLL4) that regulates cell-cell signaling (*30*) and is frequently dysregulated in cancer (*31*, *32*). GSEA showed that the expression of Notch transcriptional targets (*23*, *24*, *33*), including *MYO10*, was highly enriched in leader cells compared to follower cells (fig. S4, A and B). Among all nine Notch receptors and ligands, *JAG1* was highly expressed in leader cells compared to parental and follower cells and was by far the most differentially expressed Notch family member (Fig. 3A). Upon further interrogation, we found that *JAG1* was one of the most highly differentially expressed cell-surface ligands or receptors in the entire transcriptome analysis (Fig. 1E). We also identified *IL13RA2* as a cell-surface marker highly expressed in follower cells compared to leader cells (Fig. 1E). Flow cytometry analysis of cell-surface JAG1 revealed that the parental H1299 cell line contained approximately 7% JAG1^{HIGH}/IL13RA2$^-$ cells (fig. S4C). Consistent with RNA-seq data, leader cells were enriched in JAG1, whereas less than 1% of follower cells expressed cell-surface JAG1 (fig. S4C). In addition, when we analyzed patient-derived NSCLC primary cells (EUH3174) by flow cytometry, we saw a small population of JAG1^{HIGH}/IL13RA2$^-$ cells (~10%) and a small population of JAG1^{LOW}/IL13RA2$^+$ cells (~3%) (fig. S4C). When we assessed protein expression by immunoblotting, both MYO10 and the JAG1 full-length protein were enriched in the leader population compared to their follower counterparts, while IL13RA2 protein expression was absent in leader cells (Fig. 3B). Parental cells that were fluorescence-activated cell sorting (FACS) sorted for the "leader-like" JAG1^{HIGH}/IL13RA2$^-$ or "follower-like" JAG1^{LOW}/IL13RA2$^+$ subpopulations showed similar expression patterns of MYO10, JAG1 full-length protein, JAG1 intracellular domain (ICD), and IL13RA2 as leader cells and follower cells, respectively (Fig. 3B and fig. S4D). When we assessed JAG1 localization during 3D invasion, we confirmed that JAG1 was expressed in leaders but not followers during spheroid collective invasion (Fig. 3C). When we compared MYO10 and JAG1 localizations in leader cells cultured in either 2D or 3D, JAG1 was primarily localized to cell-cell boundaries, while MYO10 was predominantly found at the tips of the filopodia; both proteins could also be found within the cell body (fig. S5).

To determine whether JAG1 was necessary for leader cell–driven collective invasion, we performed short hairpin RNA (shRNA) knockdowns of *JAG1* in purified leader cells (Fig. 3, D and E, and fig. S6A). While reducing *JAG1* expression only moderately decreased leader cell invasion in homogenous leader-only spheroids due to poor cell-cell adhesion within the spheroid, heterogeneous spheroids consisting of 10% leader cells and 90% follower cells showed greatly decreased spheroid collective invasion (fig. S6B); similar results were observed with leader-like JAG1^{HIGH}–sorted cells alone or mixed with follower-like JAG1^{LOW}–sorted H1299 cells (fig. S6C). Likewise, JAG1 antibody inhibition decreased spheroid collective invasion and transwell invasion of multiple NSCLC cell lines and spheroids of patient-derived NSCLC primary cells EUH3174 (fig. S7, A and B). Together, these data suggest that JAG1 activity is necessary for rare leader cells within heterogeneous tumor populations to drive collective invasion.

JAG1 signaling up-regulates MYO10 expression
We next investigated whether JAG1 regulates *MYO10* expression. *JAG1* knockdown in leader cells significantly abrogated MYO10 mRNA and protein expression (Fig. 3, D and E, fig. S6A), but *MYO10* knockdown did not affect *JAG1* expression (fig. S7C). Ectopic *JAG1* overexpression in follower cells, where the *MYO10* promoter remained methylated, did not induce *MYO10* expression (Fig. 3F and fig. S7D) or alter *MYO10* promoter methylation (Fig. 3G), suggesting that JAG1 cannot restore *MYO10* expression without additional epigenetic events (e.g., promoter hypomethylation) observed in leader cells (Fig. 1). These data suggest that JAG1 is necessary for regulating *MYO10* expression in leader cells in conjunction with a permissive DNA methylation state.

Since JAG1 critically regulates 3D collective invasion and also up-regulates *MYO10* expression in leader cells, and since MYO10 drives filopodia elongation necessary for collective invasion, we predicted that the effects of JAG1 during collective invasion were mediated by its effects on filopodia via inducing *MYO10* expression. To determine whether JAG1 affects filopodia elongation, we quantified filopodia length after manipulating *MYO10* and *JAG1* expression (Fig. 3, H and I). While *JAG1* knockdown in leader cells considerably shortened filopodia, filopodial length was rescued with ectopic expression of *MYO10* (Fig. 3H). Filopodia length in follower cells increased after *JAG1* expression and further increased after expression of *MYO10* (Fig. 3I). Next, we assessed whether JAG1 regulation of *MYO10* expression affected not only filopodia length but also 3D invasion (Fig. 3, J and K). *JAG1* knockdown in leader cells abrogated spheroid collective invasion, while *MYO10* expression rescued spheroid invasion (Fig. 3J) and transwell invasion (fig. S7E). While ectopic expression of *JAG1* alone in follower cells only moderately increased spheroid collective invasion, the expression of *MYO10* in followers with or without *JAG1* substantially increased spheroid collective invasion (Fig. 3K) and transwell invasion (fig. S7E), far more than *JAG1* alone. These data strongly suggest that JAG1 regulates *MYO10* expression (and consequently filopodia length and 3D collective invasion) in epigenetically permissive leader cells.

MYO10 regulates ECM remodeling in leader cells through fibronectin micropatterning
Increased fibronectin (FN) expression correlates with cancer cell invasion and metastasis, and linearized FN promotes the directional
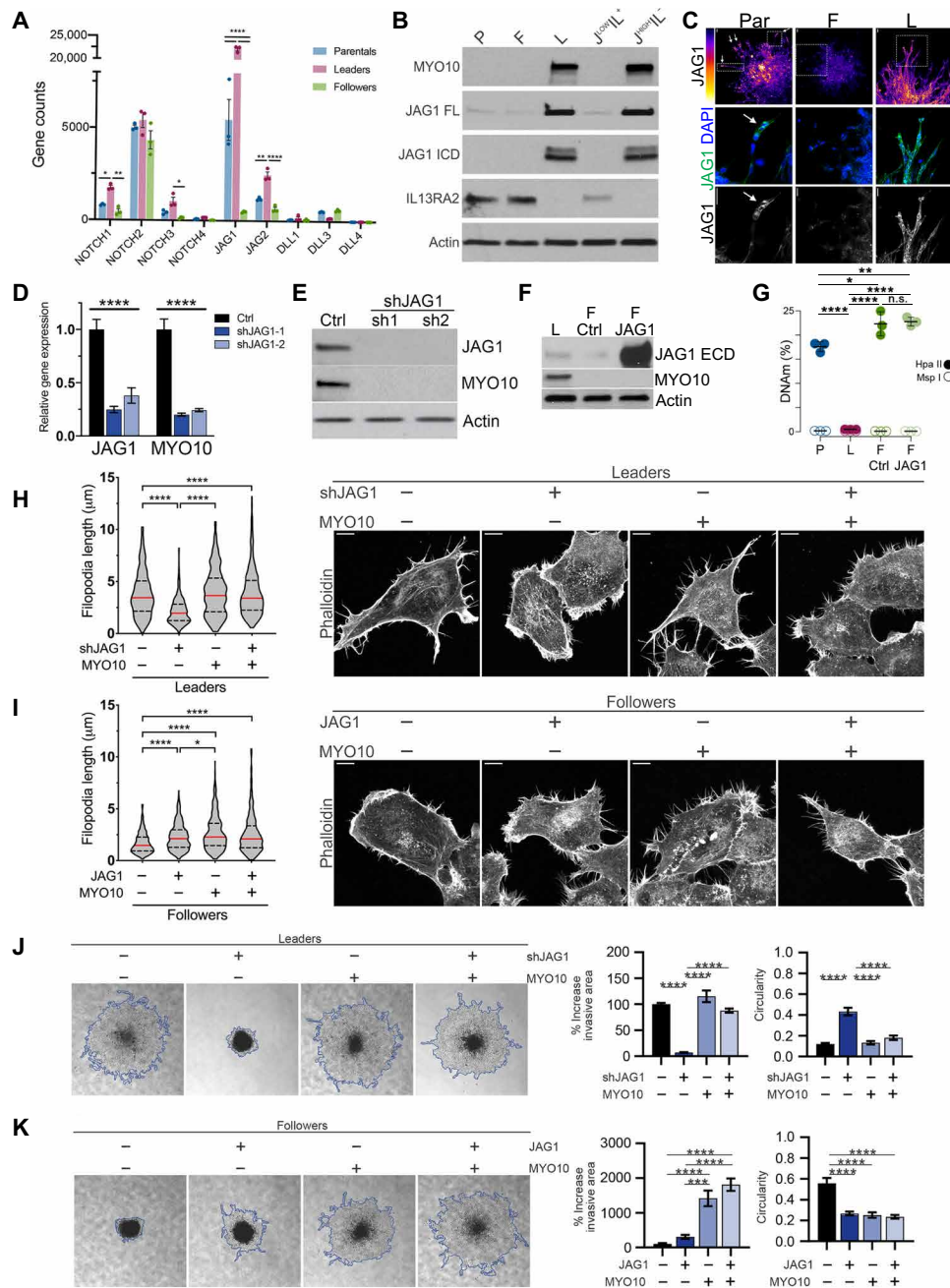
Fig. 3. JAG1 signaling is upstream of MYO10 expression in leader cells. (**A**) RNA-seq normalized gene counts for the canonical Notch receptors and ligands. Ordinary two-way ANOVA with Tukey's correction. $n = 3$. (**B**) Western blots, H1299 parental, follower, and leader cells and H1299 cells FACS sorted for JAG1-low/IL13RA2$^+$ (J^{LOW}IL$^+$) or JAG1-high/IL13RA2$^-$ (J^{HIGH}IL$^-$). Probed for MYO10, JAG1 full-length (FL), JAG1 intracellular domain (ICD), and IL13RA2. $n = 3$. (**C**) JAG1 immunofluorescence of 3D invasion of H1299 parental, follower, or leader cell spheroids. Scale bars, 50 μm. $n = 3$. (**D**) qPCR, leader cell mRNA expressing shCtrl or shJAG1, normalized to actin. $n = 3$. (**E**) Western blots of JAG1 and MYO10 expressions in H1299 leaders expressing shCtrl or shJAG1. $n = 3$. (**F**) Western blots of JAG1 and MYO10 in H1299 leaders (L), followers expressing an empty vector (F Ctrl) or JAG1 (F JAG1). $n = 4$. (**G**) Quantification of MYO10 methylation status using qPCR. $n = 3$. (**H** and **I**) Violin plots quantifying 2D filopodia length with representative images of leader cell filopodia in leaders expressing shRNA-JAG1 and/or mCherry-MYO10 (H) or followers expressing JAG1 and/or mCherry-MYO10 (I), $n = 2$, Kruskal-Wallis test with Dunn's multiple comparison test. Scale bars, 10 μm. (**J**) 3D spheroid invasion of leaders expressing shRNA-JAG1 and/or mCherry-MYO10. $n = 4$. (**K**) Representative images and quantification of 3D collective spheroid invasion follower cells expressing JAG1 and/or mCherry-MYO10. $n = 3$. (B, E, and F) Actin as loading control. (D, G, J, and K) Ordinary one-way ANOVA with Tukey's correction. (A to K) n.s., not significant; $*P < 0.05$, $**P < 0.01$, $***P < 0.001$, and $****P < 0.0001$.

migration of cancer cells (*34–36*). Our data showed that leader cells but not follower cells produced and secreted high levels of FN1 (Fig. 4, A and B) (*10*), and FN1 was the most abundant secreted protein detected in serum-free leader-conditioned media by liquid chromatography–mass spectrometry (LC-MS/MS) (Fig. 4C and data file S1). In addition to producing and secreting FN, leader cells actively remodeled extracellular FN during collective invasion into parallel linear fibrils extending past the leading edge (Figs. 4, D to G, and 5A), resembling
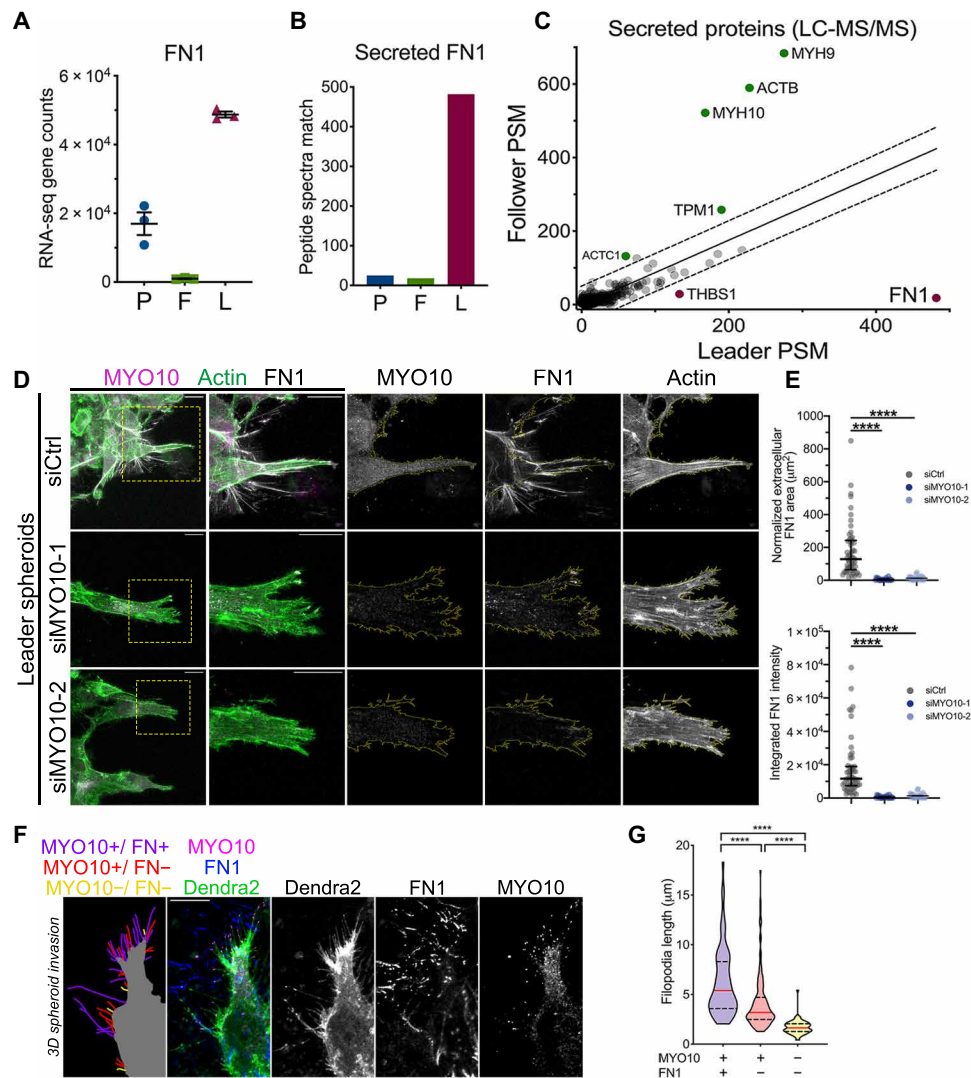
Fig. 4. MYO10 regulates alignment of extracellular FN at the leading edge of 3D invasion. (**A**) RNA-seq gene counts of FN (FN1) in parental (P), follower (F), and leader (L) cells. Ordinary one-way ANOVA with Tukey's correction. (**B**) Peptide spectra match (PSM) semiquantitative count for FN1 detected by liquid chromatography–mass spectrometry (LC-MS/MS) in media collected from parental, follower, and leader cells. $n = 1$ replicate per condition. (**C**) Scatter plot of PSM values for all peptides identified by LC-MS/MS secreted by leader (magenta) or follower (green) cells. Diagonal line indicates linear regression ($R^2 = 0.45$); dashed lines indicate 95% prediction bands. PSMs shown are the sum of all isoforms for each protein minus the PSM for serum-free RPMI 1640 alone. $n = 1$ replicate per condition. (**D**) Immunofluorescence imaging of MYO10 and FN1 in spheroid invasion assays of leader cells expressing a control siRNA or MYO10 siRNA. Actin stained with phalloidin. Scale bars, 10 μm. (**E**) Quantification of extracellular FN1 immunofluorescence signal in (**D**). For siCtrl: $n = 5$. For siMYO10-1: $n = 2$. For siMYO10-2: $n = 3$. Kruskal-Wallis test with Dunn's multiple comparison test. (**F**) Immunofluorescence imaging of leader cell spheroid invasion assays. Scale bar, 5 μm. (**G**) Violin plot of quantification of filopodia length for leader cell filopodia associated with MYO10 and/or FN1. $n = 3$. Kruskal-Wallis test with Dunn's multiple comparison test. (A to G): *$P < 0.05$, **$P < 0.01$, ***$P < 0.001$, and ****$P < 0.0001$.

invasion-promoting stromal FN alignment observed at the edges of invasive tumors (*36*, *37*). Since follower cells do not produce or secrete FN, follower cell spheroids in recombinant basement membrane (rBM) did not display any FN fibrils (Fig. 5B). Even when FN was added to the rBM, follower cell spheroids were not able to align the exogenous FN (Fig. 5C), suggesting that follower cells lack the ability to remodel extracellular FN. Leader cell FN alignment at the invasive front was also observed in invading spheroids of H1299, H1792, and H1975 cells, and EUH3174 patient-derived cells (fig. S8). Thus, NSCLC leader cells not only produced and secreted FN but also aligned this FN toward the direction of collective invasion.

Since the linear FN fibrils uniquely produced by leader cells resembled the geometry of filopodia, we hypothesized that MYO10-driven filopodia regulate FN remodeling. In support of this hypothesis, invading spheroids of MYO10-knockdown leader cells still produced FN fibrils directly underneath cell bodies but created markedly fewer extracellular FN fibrils extending past the cellular leading edge (Fig. 4, D and E). Similarly, since JAG1 promotes *MYO10* expression in leader cells, invading spheroids of *JAG1*-knockdown leader cells did not produce any FN fibrils, despite these cells producing abundant globular FN inside cell bodies and coating the extracellular surface (fig. S9). Furthermore, leader cell filopodia that
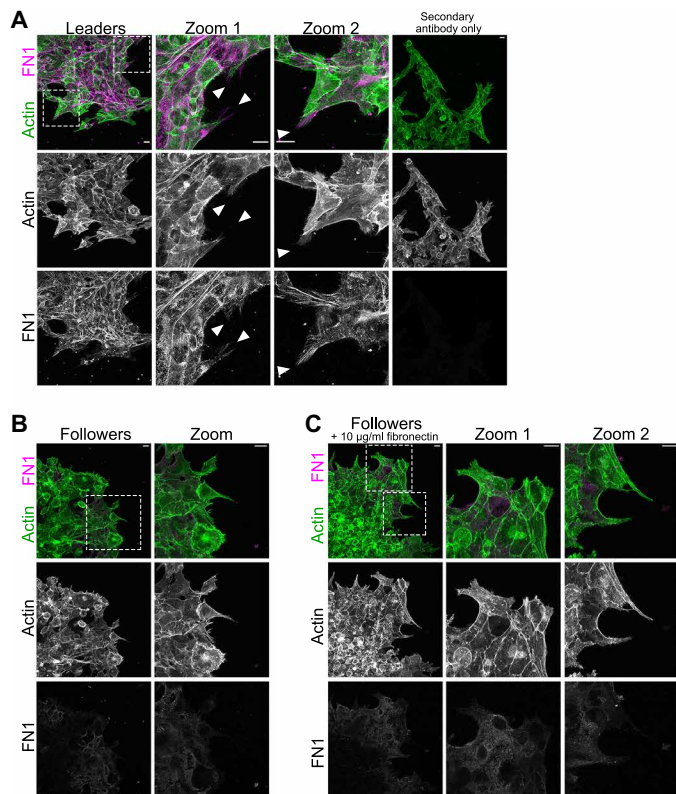
Fig. 5. Follower cells lack the ability to align extracellular FN. (**A**) Representative FN1 immunofluorescence image and optical zooms of a H1299 leader cell spheroid invading through Matrigel. Actin was stained with phalloidin. Box indicates location of zoom. Arrowheads indicate locations of linear extracellular FN micropatterning (**B**) Representative FN1 immunofluorescence images and optical zoom of a representative H1299 follower cell spheroid cultured in Matrigel. (**C**) Representative FN1 immunofluorescence images and optical zoom of a H1299 follower cell spheroid cultured in Matrigel mixed with human plasma FN (10 μg/ml). (A to C) Box indicates location of zoom. $n = 3$, $N = 18$ spheroids imaged per condition. Scale bars, 20 μm.

colocalized with MYO10 and/or FN1 during 3D invasion were considerably longer than filopodia not colocalized with either protein (Fig. 4, F and G). Therefore, these data suggest that MYO10-rich filopodia are necessary for aligning and discretely micropatterning the leading-edge extracellular FN into linearized fibrils.

MYO10 drives filopodia persistence necessary for leading-edge FN micropatterning

To investigate the interplay between MYO10-driven filopodia and FN micropatterning during collective invasion, we performed live-cell confocal imaging of leader cell spheroids expressing membrane-bound Dendra2 that were embedded into Matrigel mixed with fluorescently labeled FN (FN-rhodamine; Fig. 6, A to C, and movie S3). FN-rhodamine fibrils formed either underneath the cell body or within linearized "tracks" extending beyond the leading cell (Fig. 6A, arrows), as observed in fixed spheroids with endogenous FN (Figs. 4, D to G, and 5A and figs. S8 and S9). When assessing how filopodia and FN interacted during fibrillogenesis, we observed that leading-edge FN fibrils formed almost exclusively with ultrastable filopodia with long lifetimes in a two-step process of initiation and elongation. After a filopodium tip paused without retraction for
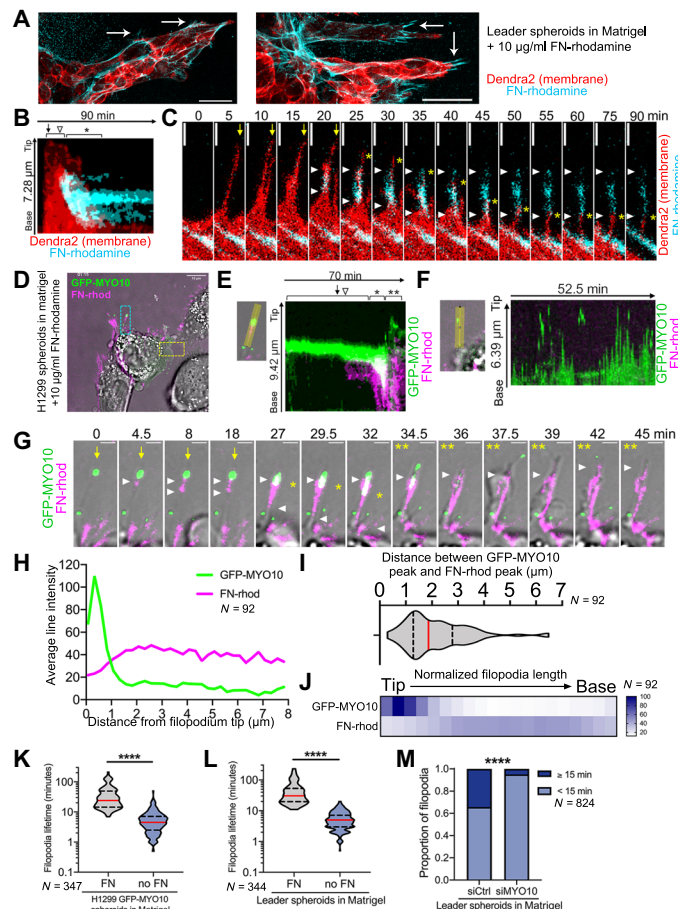

Fig. 6. MYO10 drives leader cell filopodia persistence and FN micropatterning during 3D collective invasion. (**A**) Live-cell imaging, leader cell spheroid expressing membrane-bound Dendra2 (red) embedded into rBM + FN-rhodamine (10 μg/ml) (cyan). Arrows, linear FN micropatterning. Scale bar, 50 μm. (**B** and **C**) Representative kymograph (B) and time lapse (C) of a single filopodium. Arrow, filopodium tip pause; arrowhead, nascent FN fibril appears; asterisk, filopodia retraction. Scale bars, 2 μm. (A to C) $n = 5$, $N = 112$. (**D**) Live-cell image, H1299 cell spheroids expressing GFP-MYO10 (green) embedded into rBM + FN-rhodamine (10 μg/ml) (magenta). Cyan box, zoom in of (**E**); yellow box, zoom in of (**F**). Scale bar, 10 μm. (**G**) Time lapse of the filopodium in (E). Arrow, filopodium pause; arrowheads, boundaries of nascent FN puncta; asterisk, filopodia retraction; double asterisk, second extension of the filopodia. Scale bars, 2 μm. (**H**) Line plot of average fluorescence intensity of GFP-MYO10 and FN-rhodamine along H1299 GFP-MYO10 filopodia during invasion. (**I**) Violin plot of distance (in micrometer) between the peaks of MYO10-GFP and FN-rhodamine intensity. (**J**) Heat map of distance-normalized line plot intensity values. (D to J) $n = 5$, $N = 92$. (**K** and **L**) Violin plots of filopodia lifetimes from H1299 GFP-MYO10 spheroids, $n = 4$, $N = 347$ (K); or leader cell spheroids, $n = 3$, $N = 344$ (L), comparing filopodia associated with FN-rhodamine fibrillogenesis and filopodia that were not. Mann-Whitney U test, two-tailed. (**M**) Proportion of filopodia lifetimes, leader cells expressing siCtrl or siMYO10. Two-tailed Fisher's exact test. $n = 3$, $N = 824$. (A to M) $N =$ number of filopodia, $*P < 0.05$, $**P < 0.01$, $***P < 0.001$, and $****P < 0.0001$.

several minutes (Fig. 6, B and C, arrow), FN-rhodamine nucleation puncta initiated ~2 μm behind the filopodium tip (Fig. 6, B and C, arrowheads). After the filopodium retracted toward the cell body (Fig. 6, B and C, asterisk), the distal end of FN fibrils remained in place, whereas the proximal end continued to grow and elongate. After this, some filopodia fully retracted into the cell body, and, in

other cases, the filopodia remained engaged with the fibril proximal end; in either scenario, the FN fibril remained in place, now protruding beyond the cellular leading edge along the path where the filopodia once extended and retracted (Fig. 6, B and C). Thus, these data suggest that leader cell filopodia are not merely sensors of the extracellular environment but also actively participate in FN fibrillogenesis.

To determine MYO10 localization and function during filopodia-based FN fibrillogenesis, we performed similar imaging using spheroids of H1299 cells expressing green fluorescent protein (GFP)–*MYO10* embedded into rBM mixed with FN-rhodamine (Fig. 6, D to K, and movie S4). We observed two distinct populations of GFP-MYO10 filopodia: long-lived filopodia wherein the tip persisted in one location for ≥15 min (Fig. 6, D, E, and G) and short-lived filopodia that did not persist in one location (Fig. 6F). Filopodia-associated FN fibrils initiated exclusively with long-lived filopodia, following the same two-step process of fibril initiation within the filopodia shaft and subsequent fibril elongation when filopodia retracted (Fig. 6, E to G). To quantify the spatial relationship between GFP-MYO10 and FN-rhodamine during this process, we drew line plots along the full length of 92 filopodia from tip to base at the moment when a new FN-rhodamine fibril was first visible. As expected, GFP-MYO10 localized to the filopodia tips, whereas the average FN-rhodamine intensity peaked around 2- to 2.5-μm away from the tip and then slowly tapered in intensity toward the base (Fig. 6H). The distance between the peaks of GFP-MYO10 and FN-rhodamine for each individual filopodium at the start of fibril initiation ranged from 0.3 to 6.5 μm, with a median distance of 1.8 μm (Fig. 6I). Since the length of leader cell filopodia during 3D invasion varies from approximately 2 to 20 μm (Fig. 2A), we normalized the fluorescence signal intensities across a common distance from tip to base, which showed that GFP-MYO10 localized exclusively to the filopodia tip, while FN fibrils formed along the shaft (Fig. 6J). These data were also consistent with our observations that nascent FN puncta formed within the shafts of filopodia in cells expressing membrane-bound Dendra2 (Fig. 6, B and C). Thus, these data suggest that MYO10 does not directly interact with FN but instead facilitates filopodia tip anchoring before FN fibrillogenesis begins, presumably within nascent adhesion sites along the filopodia shaft.

We observed two distinct pools of filopodia. In contrast to the long-lived filopodia associated with leading-edge FN fibrillogenesis, we observed short-lived filopodia that did not adhere to the matrix and would extend and retract multiple times without forming FN fibrils (Fig. 6F). Since only a subset of the observed filopodia formed FN fibrils, we compared the lifetimes of several hundred filopodia that either formed FN fibrils or did not form fibrils during collective spheroid invasion (Fig. 6, K and L). In spheroids of H1299 cells expressing GFP-MYO10, filopodia that formed nascent FN fibrils displayed notably long lifetimes (mean lifetime, 37.2 min) compared to filopodia that did not participate in FN fibrillogenesis (mean lifetime, 5.77 min) (Fig. 6K). Similarly, filopodia in leader cell spheroids that formed FN fibrils were ultrastable (mean lifetime, 46.3 min) compared to filopodia that did not form FN fibrils (mean lifetime, 5.6 min) (Fig. 6L). Ninety-five percent of FN fibril–producing filopodia in leader cells persisted for 15 min or longer (Fig. 6L). Thus, our data suggest that leader cells display both long-lived and short-lived subsets of filopodia during 3D collective invasion, and that only long-lived filopodia are capable of directing FN fibrillogenesis at the leading edge.

Since *MYO10* knockdown considerably shortened the mean leader cell filopodia lifetime during the 3D collective invasion from 16 to 5 min (Fig. 2C), we hypothesized that the *MYO10* knockdown specifically depleted the long-lived pool of filopodia. When we reexamined the filopodial lifetimes in siCtrl and siMYO10 leader spheroids for the presence of ultrastable filopodia, we observed that 35% of all siCtrl leader cell filopodia persisted for ≥15 min, but less than 5% of the total filopodia in *MYO10*-knockdown cells persisted for this length of time (Fig. 6M). Together, these data suggest MYO10 drives filopodial persistence for periods of time greater than 15 min, which is a necessary prerequisite for leading-edge FN fibrillogenesis to occur within the shafts of filopodia (fig. S10).

DISCUSSION

Intratumor heterogeneity drives tumor progression and metastasis, but the epigenetic contribution to this heterogeneity remains largely unexplored. Here, we found that lung cancer leader cells are a distinct population with unique patterns of both DNA methylation and gene expression compared to follower cells and the parental population (Fig. 1 and fig. S1). DNA methylation patterns that differed in leader cells compared to follower cells and parental cells correlated with a gene expression program enriched for pathways that drive collective invasion; these pathways included Notch signaling, angiogenesis, and cell-ECM interactions (Fig. 1 and fig. S2) (*4*, *5*, *10*, *21*, *38*, *39*). In contrast, follower cells and the parental population had nearly identical DNA methylation patterns despite maintaining differences in gene expression (Fig. 1). Together, these data suggest that the leader cell phenotype is characterized by a distinct epigenome, providing the first evidence of heritable epigenetic rewiring that differentiates leader and follower cells beyond gene expression alone.

We identified *MYO10* as a key gene at the intersection of differential DNA methylation and expression in leader cells (Fig. 2 and fig. S3). MYO10 is an unconventional myosin that regulates the formation and elongation of filopodia and other actin-based protrusions that are important for cancer invasion, such as filopodia-like long protrusions and invadopodia (*16*). *MYO10* loss in mice leads to severe developmental defects in several collective migration–dependent processes (*40*–*42*), which suggests that MYO10 regulates collective migration in development and cancer. We show that MYO10 is enriched in leader cells across multiple NSCLC cell lines and a patient-derived lung NSCLC cell line, and we further demonstrate that MYO10-driven filopodia are critical for leader-driven lung cancer collective invasion (Fig. 3). In addition, *MYO10* overexpression is sufficient to induce follower cell collective invasion (Fig. 3). We show how MYO10 affects filopodia elongation in a 3D ECM (Figs. 5 and 6). While MYO10-driven effects on filopodia have been well documented on 2D surfaces (*16*), we provide some of the first analysis of filopodia length and dynamics within 3D collective cancer invasion. In addition, while MYO10 has been shown to regulate cancer cell invasion and metastasis (*42*–*44*), we present the first evidence that MYO10 expression in only a rare subset of cells (i.e., leader cells) rather than the entire population is sufficient to induce tumor cell collective invasion.

Transcriptional regulation of *MYO10* is poorly understood, and our results support the model that both promoter DNA hypomethylation and JAG1/Notch transcriptional activity cooperate to drive *MYO10* expression in leader cells. We identify the Notch ligand, JAG1, as a leader-specific marker and as a transcriptional activator of *MYO10*

(Fig. 3 and figs. S4 to S7). JAG1 was detected in the rare leader cell population not only during spheroid collective invasion (Fig. 3), but it was also detected by flow cytometry within a small population of the parental H1299 cell line and within a rare subpopulation of a patient-derived NSCLC sample (fig. S4). JAG1 knockdown or inhibition greatly abrogated collective 3D invasion of several cell lines, the patient-derived sample, and mixed populations of leader and follower cells (Fig. 3 and figs. S6 and S7). In many cancers, JAG1 expression promotes cancer stem cells, tumor invasion, metastasis, and poor patient outcome (31, 45). JAG1 is also highly expressed in breast cancer leader cells (4), suggesting that JAG1 may regulate leader cells across other cancer types beyond breast and lung cancer.

Notch pathway signaling and downstream transcriptional targets are strongly enriched in leader cells compared to follower cells (figs. S1, S2, and S4), but JAG1 was the Notch family member most robustly up-regulated in leader cells (Fig. 3). We demonstrate that JAG1 up-regulates MYO10 expression; JAG1 knockdown significantly decreased MYO10 mRNA and protein expression, whereas MYO10 knockdown did not affect JAG1 expression (Fig. 3 and figs. S6 and S7), suggesting that JAG1 is upstream of MYO10. We show that JAG1 knockdown also decreased filopodia length, consistent with a loss of MYO10 expression (Fig. 3). JAG1 overexpression in follower cells did not induce MYO10 expression (Fig. 3 and fig. S7). These data suggest that JAG1 expression without other subsequent epigenetic changes to chromatin availability observed in leader cells (e.g., MYO10 promoter DNA hypomethylation) is not sufficient to induce MYO10 expression. In addition, since JAG1 was frequently present in clusters of 2 to 4 leaders within invading parental spheroids (Fig. 3), Notch signaling gene sets were significantly enriched in leaders compared to followers (figs. S1, S2, and S4), and JAG1 was strongly localized to cell-cell contacts between leader cells (fig. S5), we propose that leader cells participate in transactivation of JAG1 and Notch across two adjacent leader cells, rather than between leader and follower cells. Notch signaling often undergoes context-dependent spatiotemporal regulation (30, 46), and therefore, questions remain about how Notch/JAG1 interact to coordinate transcription within the collective invasion pack.

Cell-ECM interactions regulate several aspects of collective cancer invasion, including integrin-focal adhesion kinase motility signaling, matrix metalloproteinase–driven proteolysis of the ECM, and deposition and remodeling of ECM components (38, 39). Here, we show that leader cells but not follower cells secrete and align FN into long linear fibrils extending past the leading edge (Fig. 5). FN fibrillogenesis is a complex process that involves integrin engagement with soluble FN dimers, reorganization of the actin cytoskeleton, and translocation of integrin-FN complexes along actin filaments to form mature fibrillar adhesions (47, 48). Studies of FN fibrillogenesis have focused primarily on adhesion sites within the cell body, but questions remain as to how the fibrillogenesis that we observed within the shafts of filopodia at the leading edge of 3D invasion differs from canonical fibrillogenesis along the basal surface of the cell body.

Cell-ECM adhesion sites can form within filopodia tips or shafts, but the core components of these nascent filopodia adhesions lack many proteins that transmit traction forces seen in canonical focal adhesions or mature fibrillar adhesions (49). Nascent filopodia adhesions can mature into focal adhesions after lamellipodial advancement (29). Our live-cell imaging shows that while most FN fibrillogenesis occurred beneath the basal surface of the cell body in advancing leader cells, FN fibrillogenesis could catalyze within the shaft of stabilized MYO10-expressing filopodia (Fig. 6 and movies S3 and S4). Concomitant with filopodia tip retraction, nascent FN puncta elongated from the proximal end of the fibril, while the distal end remained in place. In many cases, the distal end of the FN fibril remained anchored to the ECM, while the proximal end of the FN fibril continued to elongate under the cell body even after the filopodia completely retracted, leaving long FN tracks extending in front of the leading cell, parallel to the direction of collective invasion (Fig. 6). This observation of multistep FN fibril elongation is consistent with focal adhesions maturing into fibrillar adhesions during FN fibrillogenesis observed underneath the basal surface of the cell body (47). However, these nascent filopodial adhesions likely differ from canonical focal adhesions in their integrin and intracellular components (29, 49). Understanding how these filopodial adhesions mature into focal adhesions and how they transmit traction forces capable of remodeling the ECM (i.e., FN fibrillogenesis) remain areas of keen interest.

Notably, nascent FN fibrils initiated approximately 1.8 μm behind the filopodia tip and were not colocalized with MYO10-GFP in live-cell imaging (Fig. 6). This suggests that MYO10 is not directly interacting with FN. However, MYO10+ leader cell filopodia had a longer lifetime than MYO10-knockdown filopodia during 3D invasion (Fig. 6). We speculate that MYO10-driven filopodial persistence is necessary for forming nascent filopodial adhesions in the tip and/or shaft, engaging with FN, and maturing into larger focal adhesion sites capable of elongating nascent FN fibrils at the leading edge. Thus, in MYO10-knockdown cells, FN fibrillogenesis can still occasionally be seen beneath the cell body (Fig. 4), but MYO10-depleted cells form strikingly fewer leading-edge FN tracks since these filopodia likely do not persist long enough to form nascent adhesions (Figs. 4 and 6). Further studies of traction forces within filopodia, how integrin activation and molecular components differ between filopodial tip and shaft adhesions, and how filopodial tip adhesions and shaft adhesions differentially affect filopodial dynamics and FN fibrillogenesis may elucidate how filopodia act not only as sensors of the extracellular environment but also as active participants in ECM remodeling.

While leader-specific shifts in DNA methylation and gene expression (e.g., high expression of MYO10 and JAG1) were significant when comparing an isolated leader cell population to follower or parental cells, these patterns could not be detected in the parental cell population when pooled. However, heterogeneous protein expression was detected in single cells within the parental population by flow cytometry. The parental population contained a small percentage of leader cells (10, 13); patient tumors likely also contain similar rare but genetically or epigenetically distinct cell populations that cannot be detected by bulk analysis of the whole tumor. Thus, we hypothesize that these rare tumor cell subpopulations might only be detected in patients using single-cell analysis techniques. Further improving and integrating single-cell technologies into clinical use will be critical for identifying those rare but functionally distinct tumor subpopulations driven by epigenetic heterogeneity, such as leader cells or cancer stem cells. In addition, we anticipate differences between leader and follower cell subpopulations in other epigenetic mechanisms that influence chromatin states and transcriptional regulation beyond DNA methylation. Continued exploration of intratumor genetic and epigenetic heterogeneity will be crucial for fully understanding tumor clonal evolution and its relationship to collective invasion.

MATERIALS AND METHODS

Cell culture conditions

H1299, H23, H1792, and H1975, human NSCLC cells [American Type Culture Collection (ATCC), Manassas, VA] were cultured in RPMI 1640 media supplemented with 10% fetal bovine serum (FBS) and penicillin-streptomycin (100 U ml^{-1}) and maintained at 37°C and 5% CO_2. Human embryonic kidney (HEK) 293T cells (ATCC, Manassas, VA) were maintained in Dulbecco's modified Eagle's media (DMEM) supplemented with 10% FBS and penicillin-streptomycin (100 U ml^{-1}) at 37°C and 5% CO_2. Leader and follower cell subpopulations were isolated from H1299 cells transfected with Dendra2 via SaGA, as previously described (10). Briefly, H1299 cells were transfected with plasma membrane–targeted Dendra2, a photoconvertible fluorophore, allowing for visualization of individual cells during imaging. Before photoconversion, all cells have green fluorescence (maximum excitation, 490 nm; maximum emission, 507 nm); upon excitation with a 405 nm laser, the Dendra2 within the selected cell is photoconverted to emit red fluorescence (maximum excitation, 553 nm; maximum emission, 573 nm). During 3D invasion, singular leader cells or groups of follower cells were photoconverted separately without any measurable fluorescence conversion in neighboring cells. Subsequently, the cells were extracted from the 3D matrices and sorted out using flow cytometry. All primary cells and cell lines were authenticated by ATCC (where applicable) or by analysis of morphological and phenotypic characteristics and gene and protein expression. No cell lines used in this study were found in the database of commonly misidentified cell lines that is maintained by the International Cell Line Authentication Committee and the National Center for Biotechnology Information BioSample. All primary cells and cell lines were tested for mycoplasma contamination using a commercially available kit (PCR-Mycoplasma Test Kit I/C, Promokine PK-CA91-1024), according to the manufacturer's instructions, at the onset of the work (tested negative) and have never exhibited contamination symptoms after initial testing.

NSCLC patient-derived cell line

All tissue samples were procured by the Human Tissue Procurement Service shared resource at the Winship Cancer Institute of Emory University in accordance with the approved institutional review board protocol. Tissues were digested for 3 hours in digestion buffer [DMEM/F-12 supplemented with 10 mM Hepes, 2% bovine serum albumin, 1× ITS (insulin-transferrin-selenium), hydrocortisone (0.5 µg/ml), and 1× normocin] containing type 3 collagenase (2 mg/ml; Worthington), hyaluronidase (100 U/ml; Sigma) at 37°C until fully digested. Cells were pelleted for 5 min at 300g, resuspended in red blood cell lysis buffer (Abcam) to lyse red blood cells, and pelleted again. Cells were then resuspended in digestion buffer containing deoxyribonuclease 1 (DNase 1) (200µg/ml; Sigma) and incubated for 10 min at 37°C. After DNase digestion, cells were pelleted, resuspended in media, and plated. Cells were grown in modified M87 media containing 2% FBS (50). The presence of the NSCLC marker TTF1 (EP1584Y) (1:50, Abcam) and pan-cytokeratin (clone PCK-26) (1:300, Abcam) and the absence of the fibroblast marker S100A4 (EPR2761) (1:100, Abcam) were used to verify the purity of these lines (51).

Plasmids, transfections, and transductions

Derivative cells were transfected using Lipofectamine 3000 (Thermo Fisher Scientific, Waltham, MA), per the manufacturer's instructions, or transduced using lentiviral supernatants derived from HEK 293T cells using the psPAX2-PMD2.G system. The pCMVLifeAct-TagRFP plasmid was obtained from Ibidi (Gräfelfing, Germany; 60102). The gd2PAL-Dendra2 plasmid was obtained from G. Bassell (Emory University) and transfected into H1299 cells, as previously described (10). The GFP-MYO10 and mCherry-MYO10 constructs were a gift from R. Cheney [University of North Carolina (UNC), Chapel Hill] (52). The human JAG1 shRNA (HSH004470-LVRU6P) and open reading frame (EX-M0722-Lv105-B) constructs were purchased from GeneCopoeia (Rockville, MD). The human MYO10 siRNA constructs (Silencer Select siRNA s9224 and s9225) were purchased from Thermo Fisher Scientific (Waltham, MA).

Reagents and antibodies

Primary and secondary antibodies for immunoblotting

MYO10 (Novus Biologicals, NBP1-87748) was used at 1:2000. JAG1 (Cell Signaling Technology, 70109) was used at 1:2000. IL13RA2 (Abcam, ab55275) was used at 1:2000. Cleaved Notch1 (Val1744) (Cell Signaling Technology, 4147) was used at 1:2000. α-Tubulin (Millipore, MAB1864) was used at 1:5000. Actin (Sigma, A2066) was used at 1:5000. Glyceraldehyde 3-phosphate dehydrogenase (GAPDH) (Cell Signaling Technology, 2118) was used at 1:5000. Peroxidase AffiniPure Goat Anti-Mouse immunoglobulin G (IgG) (H+L) (Jackson ImmunoResearch, 115-035-003) was used at 1:10,000. Peroxidase AffiniPure Goat Anti-Rabbit IgG (H+L) (Jackson Immuno-Research, 111-035-144) was used at 1:10,000. Peroxidase AffiniPure Goat Anti-Rat IgG (H+L) (Jackson ImmunoResearch, 112-035-003) was used at 1:10,000.

Primary and secondary antibodies and reagents for immunostaining

MYO10 (Novus Biologicals, NBP1-87748) was used at 1:1000. JAG1 (Cell Signaling Technology, 70109) was used at 1:1000. FN1 (Abcam, ab6328) was used at 1:1000. 4′,6-Diamidine-2′-phenylindole dihydrochloride (Sigma, D9542) was used as a nuclear counterstain at 300 nM. Phalloidin-488 (Thermo Fisher Scientific, A12379) or phalloidin-635 (Thermo Fisher Scientific, A34054) was dissolved in methanol and used at 1:100. Rhodamine-FN (Cytoskeleton, FNR01) was used at 1:50 and mixed with rBM. JAG1 antibody used for blocking (Sino Biological, 1164-MMO3) was used at 100 ng/ml.

Fluorophore-conjugated primary antibodies for FACS

JAG1-PE (Sino Biological, 11648-MM03-P) was used at 5 µl per 100 µl, and IL13RA2-APC (Miltenyi Biotec, 130-104-505) was used at 2 µl per 100 µl.

DNA methylation microarray and quantitative PCR

DNA methylation status was assessed in triplicate on H1299 parental, leader, and follower cells. For parental cells, three different passages were used. For follower cells, three separately isolated populations were used. For leader cells, two separately isolated populations were used: one passage of one population and two passages of the other. Cells were grown to 70% confluency and then trypsinized and homogenized using QIAshredder (Qiagen, 79654; Hilden, Germany). DNA and RNA were isolated in tandem using the AllPrep DNA/RNA Mini Kit (Qiagen, 80204). Fluorescent DNA quantification was performed using the Quant-iT double-stranded DNA broad range assay (Invitrogen, Q33130; Carlsbad, CA). Quality was assessed on a 2% agarose gel. Five hundred nanograms of DNA was bisulfite converted using the Zymo EZ-96 DNA Methylation Kit using the protocol suggested by the Illumina Infinium Methylation guide (Illumina, 150191519; San Diego, CA). The bisulfite-converted DNA was then used with the Illumina Infinium HD Methylation Assay in a whole-genome amplification (WGA). After WGA, the DNA was

fragmented, precipitated, resuspended, and hybridized to the Illumina MethylationEPIC BeadChip array (Illumina, WG-317-1001), which was then washed to remove any unbound DNA. The bound DNA underwent extension and staining according to the manufacturer protocol. The BeadChip was then coated and scanned on the Illumina HiScan to obtain the raw data.

Array data were processed and analyzed in R using the package ChAMP (53). Probe data were filtered according to the standard ChAMP settings, with the exception of not filtering out probes on the X and Y chromosomes. Beta values were normalized using the Beta-Mixture Quantile (BMIQ) method and standard settings. DMPs were determined using the champ.DMP() command, which calculates Benjamini-Hochberg–adjusted P values using the limma package. DMPs with a beta difference > 0.2 and an adjusted P <0.05 were considered significant. DMRs were determined using the champ.DMR() command, using the ProbeLasso algorithm with a minimum DMR size of 50 bp and a minimum of two probes. DMRs with a beta difference > 0.2 and an adjusted P < 0.05 were considered significant. Overlaps of DMPs or DMRs with genomic features were performed using the GenomicRanges package. GSEA of DMPs was performed using the methylGSA package, using the methylRRA method and standard settings (24). Bonferroni-adjusted P < 0.05 was considered significant. Gene sets used for enrichment analysis included the Molecular Signatures Database (MSigDB v6.2) Hallmark gene set collection, Kyoto Encyclopedia of Genes and Genomes (KEGG) Pathway Database, and Reactome Pathway Database. DMPs were annotated on the basis of their relationship with GenCode (V27, hg19) transcripts with the following hierarchy: (i) CpG within a protein-coding transcription start sites (TSS200 and TSS1500); (ii) within a protein-coding gene (intergenic); (iii) within 2 kb of a protein-coding gene (perigenic); (iv) long noncoding RNA; (v) other noncoding RNA (microRNA, ribosomal RNA, single-cell RNA, small nuclear RNA, small nucleolar RNA, ribozyme, small RNA, antisense RNA, or small Cajal body–specific RNA); and (vi) pseudogenes. All other CpGs were considered intergenic. CGIs were defined according to University of California Santa Cruz (UCSC) hg19.

DNA methylation was also quantified using the methyl-sensitive Hpa II enzyme to digest unmethylated cytosine-cytosine-guanine-guanine (CCGG) motifs, as previously described (54). Briefly, DNA was aliquoted into three equal portions of 500 ng for mock, Hpa II (40 U; New England Biolabs R0171S), and Msp I (40 U; New England Biolabs R0106S) digestion reactions with CutSmart Buffer (New England Biolabs), which were performed overnight at 37°C in a T100 thermal cycler (BioRad). qPCR primers were designed to span one CCGG site and used to quantify the DNA in each reaction. Here, the mock-digested DNA was used to quantify the total amount of DNA, the Hpa II–digested reaction represents the methylated fraction of DNA, and the methyl-insensitive isoschizomer Msp I serves as a digestion/negative control. DNA methylation levels were quantified as the ratio of Hpa II–digested material to mock-digested material. Primer sequences for all qPCR reactions are MYO10 forward (TGAGACGCTCGCATTTTCTA) and MYO10 reverse (CAGGGCCTCCGTTTTCTTAC).

RNA-seq and GSEA

RNA-seq was performed in triplicate on H1299 parental, leader, and follower cells. RNA library preparation and sequencing were performed by the Emory Integrated Genomics Core and Omega BioTek Inc., as previously described (13). Data processing, read alignment, quality control, and statistical analyses were performed by the Emory Biostatistics and Bioinformatics Shared Resource, as previously described (13). RNA-seq expression raw counts for human hg19 RefSeq annotated genes were measured using HTSeq v0.6.1 (55). Count normalization and pairwise differential analysis were determined using DESeq (56), which uses a negative binomial distribution statistic with a Benjamini-Hochberg–corrected false discovery rate. Data were log 2(normalized count + 1)–transformed for all downstream analysis. Unsupervised hierarchical clustering and the resulting heat maps were created using NOt Just Another Heatmap (57).

GSEA (23) javaGSEA desktop application was used to identify gene expression profiles that were enriched in either leader or follower cells. Gene sets were selected from the Molecular Signatures Database (MSigDB v6.2), including the Hallmark gene set collection, KEGG Pathway Database, and Reactome Pathway Database. Enrichment scores were calculated using a weighted signal-to-noise ratio with 1000 permutations and randomization by gene set to account for a small sample size (N = 3 for each cell type). Gene sets were considered significantly enriched in either leaders or followers with a normalized enrichment score > 1.5, a nominal P < 0.05, and a false discovery rate q value < 0.25.

3D invasion assays, spheroid microscopy, and image analysis

Spheroids were generated, as previously described (10), and embedded in Matrigel rBM (Corning, 356237). Images were taken using an Olympus CKX41 microscope with an Infinity 1-3C camera [×4 air, 0.13 numerical aperture (NA), UPlanFL N]. For mixed-population spheroid experiments, cells were plated together in low-adhesion wells at the indicated ratios, with 3000 total cells per spheroid. Invasive area and spheroid circularity were measured using ImageJ, as previously described (10).

Quantitative PCR

Quantitative real-time PCR was performed in triplicate with iTaq Universal SYBR Green Supermix (BioRad, catalog no.1725121) using a CFX96 real-time PCR detection system (BioRad), and the relative amount of complementary DNA was calculated using a standard dilution curve, based on human GAPDH mRNA or human tubulin mRNA. Primer sequences for all qPCR reactions are MYO10 forward (TGAGAGGGAGCTGCTCTTTG), MYO10 reverse (GTCGTGCTGTAGCGCTTCTTC), JAG1 forward (GGCAACACCTTCAACCTCAAG), JAG1 reverse (TGATCATGCCCGAGTGAGAAG), GAPDH forward (GGTGGTCTCCTCTGACTTCAACA), GAPDH reverse (GTTGCTGTAGCCAAATTCGTTGT), tubulin forward (CTTCGGCCAGATCTTCAGAC), and tubulin reverse (AGAGAGTGGGTCAGCTGGAA).

Immunoblotting and immunostaining

For immunoblotting, total cellular protein expression was assessed via western blotting. Briefly, adherent cells were rinsed twice with 1× phosphate-buffered saline (PBS) containing Ca^{2+} and Mg^{2+} and lysed with 2% SDS lysis buffer [50 mM tris (pH 8.0), 2% SDS, 100 mM NaCl, and 50 mM dithiothreitol] supplemented with Halt Protease and Phosphatase Inhibitor Cocktail (Thermo Fisher Scientific, 78442). Samples were subsequently sonicated briefly to shear the DNA and reduce lysate viscosity. Sample protein content was quantified using a bicinchoninic acid protein assay kit (Thermo Fisher Scientific, 23225) before SDS–polyacrylamide gel electrophoresis.

For immunostaining, cells in 2D or spheroids embedded in rBM were rinsed twice with 1× PBS containing calcium and magnesium prewarmed to 37°C and then immediately fixed with paraformaldehyde and glutaraldehyde (1× PBS containing calcium and magnesium with added 2% paraformaldehyde and 0.001% glutaraldehyde; freshly prepared and warmed to 37°C) for 20 min at room temperature. For immunofluorescence staining, permeabilization, three glycine rinses, blocking, and antibody staining were performed, as previously described (58). After primary and secondary antibody staining, cells in 2D or 3D spheroids were imaged with the Leica TCS SP8 inverted confocal microscope (×20 air HC PL APO CS2, 0.75 NA; ×40 oil HC PL APO CS2, 1.30 NA; and ×63 oil HC PL APO CS2, 1.40 NA) using 1-mm stack intervals for ×20 objective or 0.3-mm Z-stack intervals for all other objectives, line scanning (405-nm direct modulation Flexible, 488-nm argon, 561-nm diode-pumped solid-state, and 633-nm helium-neon), 2× line averaging, and both Hyd GaAsP detectors and photomultiplier tube detectors.

Live-cell imaging

Cells were plated into cell culture dishes with optical glass bottoms or spheroids were embedded in rBM, as previously described (10), and then imaged using the Leica TCS SP8 inverted confocal microscope (×20 air HC PL APO CS2, 0.75 NA; ×40 oil HC PL APO CS2, 1.30 NA; ×63 oil HC PL APO CS2, 1.40 NA; and ×100 oil HC PL APO CS2, 1.40 NA) with a live-cell chamber (37°C and 5% CO_2) or using 1-mm stack intervals for ×20 objective or 0.3-mm Z-stack intervals for all other objectives, line scanning using a resonant galvanometric tandem scanner (8 kHz; 488-nm argon, 561-nm DPSS, and 633-nm helium-neon), eight times line averaging, and Hyd GaAsP detectors. For LifeAct-RFP imaging of filopodia dynamics in 2D, images were acquired with the ×100 objective every second for 10 min. For cell migration tracking in 2D, images were acquired with the ×20 objective every 5 min for 16 hours. For imaging of filopodia dynamics and rhodamine-FN fibrillogenesis during 3D spheroid collective invasion, images were acquired with the ×63 objective every 30 s for approximately 1 to 2 hours.

Image analysis

Spheroid invasive area and circularity (an indirect measure of sheet-like invasion) were measured using ImageJ, as previously described (10). For immunofluorescence, all 3D images (x, y, and z) were flattened to 2D maximum projections (x and y) using ImageJ to increase the intensity of dim spheroid branches or fine filopodial structures. The maximum and minimum pixel values for each channel were thresholded to the same 8-bit values for all images within the same experiment. For 2D cell migration assays, quantification of cell migration was done using Volocity imaging software. For analysis of filopodia length in fixed 3D samples, filopodia length was manually quantified using ImageJ software. For analysis of filopodia dynamics during live 3D collective cell invasion, filopodia were manually tracked using ImageJ software.

Analysis of the localization of Dendra2, GFP-MYO10, and rhodamine-FN along filopodia during 3D collective cell invasion

The 4D images (x, y, z, and t) were reduced to a 3D maximum projection (x, y, and t) to increase the visibility of filopodia and nascent FN puncta. Quantification was performed on the time point where the nascent FN puncta were first visible. For each filopodium, a line (width = 3 pixels) was drawn on top of the filopodia from tip to base, and a line plot profile was created for each separated channel (Analyze>Plot Profile). The peak of the rhodamine-FN puncta and

the peak of GFP-MYO10 were defined as the point along the line with the highest pixel intensity. Before analysis, the correct localization of the FN nascent puncta and the end of the filopodia were each visually confirmed by examining several frames before and after the time frame represented in the line plot.

Quantification of extracellular FN area

All image analysis was performed in ImageJ. 3D images (x, y, and z) were flattened to 2D maximum projections (x and y). The phalloidin channel was used to create a binary threshold of the intracellular area using Image>Adjust>Threshold. If necessary, then any holes in the cell outline were filled with Process>Binary>Fill Holes. The binary threshold was eroded with a pixel count of three to remove background speckles (Process>Binary>Options>Count = 3 and Process>Binary>Erode). A selection was created from the remaining binary threshold encompassing the intracellular area, and the surface area was measured to normalize extracellular FN area. Next, the FN channel of the images was smoothened to reduce nonspecific background noise (Process>Smooth). Next, the intracellular selection was pasted onto the FN image, and the pixels inside of this selection were cleared (Edit>Selection>Clear), leaving behind only extracellular FN. The remaining pixels were used to create a binary threshold using the same method as above for the phalloidin channel. The area and integrated density of the extracellular FN within the threshold were measured (Analyze>Measure) and normalized to the intracellular area of the same image.

LC-MS/MS of secreted proteins

To produce serum-free conditioned media, cells were grown to 70% confluency on three 100-mm cell culture dishes per sample. The cells were then washed twice with 1× PBS and then cultured in 8 ml of serum-free RPMI 1640 for 48 hours. The collected conditioned media were centrifuged at 300g at 4°C for 15 min to remove dead cells from the media. To purify proteins secreted by the cells, 15 ml of conditioned media was transferred into an Amicon Ultra-15 Centrifugal Filter Unit with a filter size of 3 kDa and centrifuged at 4000g at 4°C for 60 min in a swinging bucket rotor. Fifteen milliliters of RPMI 1640 without serum was also concentrated using the same method. LC-MS/MS data acquisition was performed, as previously described (59), using a Dionex Ultimate 3000 RSLCNano and monitored on an Orbitrap Fusion mass spectrometer (Thermo Fisher Scientific, San Jose, CA). Analysis of MS data was performed, as previously described. Peptides were identified by matching the spectra with Proteome Discoverer 2.0 (Thermo Fisher Scientific) against the human Uniprot database (90,300 target sequences).

Statistical analysis

All quantitative results were analyzed with the test indicated in the figure legends, after confirming that the data met appropriate assumptions (normality, homogeneous variance, and independent sampling). Unless otherwise stated, all indicated P values are two tailed, and all bar graph data are plotted as the mean, with error bars indicating SEM. For all violin plots, solid red line indicates the median, and black dashed lines indicate the interquartile range. All results were reproduced at least twice in the laboratory. The figure legends indicate the number of independent biological replicates and sample size for each experiment. In all figures, n is the number of independent biological replicates. Microsoft Excel and GraphPad Prism software were used to conduct statistical analyses of the data. P values less than 0.05 were considered significant.

SUPPLEMENTARY MATERIALS

Supplementary material for this article is available at http://advances.sciencemag.org/cgi/content/full/6/30/eaaz6197/DC1

View/request a protocol for this paper from *Bio-protocol*.

REFERENCES AND NOTES

1. L. G. T. Morris, N. Riaz, A. Desrichard, Y. Şenbabaoğlu, A. A. Hakimi, V. Makarov, J. S. Reis-Filho, T. A. Chan, Pan-cancer analysis of intratumor heterogeneity as a prognostic determinant of survival. *Oncotarget* **7**, 10051–10063 (2016).

2. N. McGranahan, C. Swanton, Biological and therapeutic impact of intratumor heterogeneity in cancer evolution. *Cancer Cell* **27**, 15–26 (2015).

3. Q. Wei, Z. Ye, X. Zhong, L. Li, C. Wang, R. E. Myers, J. P. Palazzo, D. Fortuna, A. Yan, S. A. Waldman, X. Chen, J. A. Posey, A. Basu-Mallick, B. H. Jiang, L. Hou, J. Shu, Y. Sun, J. Xing, B. Li, H. Yang, Multiregion whole-exome sequencing of matched primary and metastatic tumors revealed genomic heterogeneity and suggested polyclonal seeding in colorectal cancer metastasis. *Ann. Oncol.* **28**, 2135–2141 (2017).

4. K. J. Cheung, V. Padmanaban, V. Silvestri, K. Schipper, J. D. Cohen, A. N. Fairchild, M. A. Gorin, J. E. Verdone, K. J. Pienta, J. S. Bader, A. J. Ewald, Polyclonal breast cancer metastases arise from collective dissemination of keratin 14-expressing tumor cell clusters. *Proc. Natl. Acad. Sci. U.S.A.* **113**, E854–E863 (2016).

5. M. Janiszewska, D. P. Tabassum, Z. Castaño, S. Cristea, K. N. Yamamoto, N. L. Kingston, K. C. Murphy, S. Shu, N. W. Harper, C. G. Del Alcazar, M. Alečković, M. B. Ekram, O. Cohen, M. Kwak, Y. Qin, T. Laszewski, A. Luoma, A. Marusyk, K. W. Wucherpfennig, N. Wagle, R. Fan, F. Michor, S. S. McAllister, K. Polyak, Subclonal cooperation drives metastasis by modulating local and systemic immune microenvironments. *Nat. Cell Biol.* **21**, 879–888 (2019).

6. K. J. Cheung, E. Gabrielson, Z. Werb, A. J. Ewald, Collective invasion in breast cancer requires a conserved basal epithelial program. *Cell* **155**, 1639–1651 (2013).

7. P. Friedl, J. Locker, E. Sahai, J. E. Segall, Classifying collective cancer cell invasion. *Nat. Cell Biol.* **14**, 777–783 (2012).

8. N. Aceto, A. Bardia, D. T. Miyamoto, M. C. Donaldson, B. S. Wittner, J. A. Spencer, M. Yu, A. Pely, A. Engstrom, H. Zhu, B. W. Brannigan, R. Kapur, S. L. Stott, T. Shioda, S. Ramaswamy, D. T. Ting, C. P. Lin, M. Toner, D. A. Haber, S. Maheswaran, Circulating tumor cell clusters are oligoclonal precursors of breast cancer metastasis. *Cell* **158**, 1110–1122 (2014).

9. M. Gilbert-Ross, J. Konen, J. Koo, J. Shupe, B. S. Robinson, W. G. Wiles IV, C. Huang, W. D. Martin, M. Behera, G. H. Smith, C. E. Hill, M. R. Rossi, G. L. Sica, M. Rupji, Z. Chen, J. Kowalski, A. L. Kasinski, S. S. Ramalingam, H. Fu, F. R. Khuri, W. Zhou, A. I. Marcus, Targeting adhesion signaling in KRAS, LKB1 mutant lung adenocarcinoma. *JCI Insight* **2**, e90487 (2017).

10. J. Konen, E. Summerbell, B. Dwivedi, K. Galior, Y. Hou, L. Rusnak, A. Chen, J. Saltz, W. Zhou, L. H. Boise, P. Vertino, L. Cooper, K. Salaita, J. Kowalski, A. I. Marcus, Image-guided genomics of phenotypically heterogeneous populations reveals vascular signalling during symbiotic collective cancer invasion. *Nat. Commun.* **8**, 15078 (2017).

11. P. Friedl, P. B. Noble, P. A. Walton, D. W. Laird, P. J. Chauvin, R. J. Tabah, M. Black, K. S. Zänker, Migration of coordinated cell clusters in mesenchymal and epithelial cancer explants in vitro. *Cancer Res.* **55**, 4557–4560 (1995).

12. J. M. Westcott, A. M. Prechtl, E. A. Maine, T. T. Dang, M. A. Esparza, H. Sun, Y. Zhou, Y. Xie, G. W. Pearson, An epigenetically distinct breast cancer cell subpopulation promotes collective invasion. *J. Clin. Invest.* **125**, 1927–1943 (2015).

13. E. L. Zoeller, B. Pedro, J. Konen, B. Dwivedi, M. Rupji, N. Sundararaman, L. Wang, J. R. Horton, C. Zhong, B. G. Barwick, X. Cheng, E. D. Martinez, M. P. Torres, J. Kowalski, A. I. Marcus, P. M. Vertino, Genetic heterogeneity within collective invasion packs drives leader and follower cell phenotypes. *J. Cell Sci.* **132**, jcs231514 (2019).

14. E. Wagenblast, M. Soto, S. Gutiérrez-Ángel, C. A. Hartl, A. L. Gable, A. R. Maceli, N. Erard, A. M. Williams, S. Y. Kim, S. Dickopf, J. C. Harrell, A. D. Smith, C. M. Perou, J. E. Wilkinson, G. J. Hannon, S. R. V. Knott, A model of breast cancer heterogeneity reveals vascular mimicry as a driver of metastasis. *Nature* **520**, 358–362 (2015).

15. G. Jacquemet, H. Hamidi, J. Ivaska, Filopodia in cell adhesion, 3D migration and cancer cell invasion. *Curr. Opin. Cell Biol.* **36**, 23–31 (2015).

16. A. B. Bohil, B. W. Robertson, R. E. Cheney, Myosin-X is a molecular motor that functions in filopodia formation. *Proc. Natl. Acad. Sci. U.S.A.* **103**, 12411–12416 (2006).

17. H. Zhang, J. S. Berg, Z. Li, Y. Wang, P. Lång, A. D. Sousa, A. Bhaskar, R. E. Cheney, S. Strömblad, Myosin-X provides a motor-based link between integrins and the cytoskeleton. *Nat. Cell Biol.* **6**, 523–531 (2004).

18. Y. Hirano, T. Hatano, A. Takahashi, M. Toriyama, N. Inagaki, T. Hakoshima, Structural basis of cargo recognition by the myosin-X MyTH₄-FERM domain. *EMBO J.* **30**, 2734–2747 (2011).

19. S. B. Baylin, P. A. Jones, A decade of exploring the cancer epigenome–Biological and translational implications. *Nat. Rev. Cancer* **11**, 726–734 (2011).

20. ENCODE Project Consortium, An integrated encyclopedia of DNA elements in the human genome. *Nature* **489**, 57–74 (2012).

21. J. B. Long, S. M. Jay, S. S. Segal, J. A. Madri, VEGF-A and Semaphorin3A: Modulators of vascular sympathetic innervation. *Dev. Biol.* **334**, 119–132 (2009).

22. Q. Raza, J. R. Jacobs, Guidance signalling regulates leading edge behaviour during collective cell migration of cardiac cells in Drosophila. *Dev. Biol.* **419**, 285–297 (2016).

23. A. Subramanian, P. Tamayo, V. K. Mootha, S. Mukherjee, B. L. Ebert, M. A. Gillette, A. Paulovich, S. L. Pomeroy, T. R. Golub, E. S. Lander, J. P. Mesirov, Gene set enrichment analysis: A knowledge-based approach for interpreting genome-wide expression profiles. *Proc. Natl. Acad. Sci. U.S.A.* **102**, 15545–15550 (2005).

24. X. Ren, P. F. Kuan, methylGSA: A Bioconductor package and Shiny app for DNA methylation data length bias adjustment in gene set testing. *Bioinformatics* **35**, 1958–1959 (2019).

25. K. He, T. Sakai, Y. Tsukasaki, T. M. Watanabe, M. Ikebe, Myosin X is recruited to nascent focal adhesions at the leading edge and induces multi-cycle filopodial elongation. *Sci. Rep.* **7**, 13685 (2017).

26. M. P. Ball, J. B. Li, Y. Gao, J.-H. Lee, E. M. LeProust, I.-H. Park, B. Xie, G. Q. Daley, G. M. Church, Targeted and genome-scale strategies reveal gene-body methylation signatures in human cells. *Nat. Biotechnol.* **27**, 361–368 (2009).

27. N. O. Alieva, A. K. Efremov, S. Hu, D. Oh, Z. Chen, M. Natarajan, H. T. Ong, A. Jégou, G. Romet-Lemonne, J. T. Groves, M. P. Sheetz, J. Yan, A. D. Bershadsky, Myosin IIA and formin dependent mechanosensitivity of filopodia adhesion. *Nat. Commun.* **10**, 3593 (2019).

28. G. Jacquemet, H. Baghirov, M. Georgiadou, H. Sihto, E. Peuhu, P. Cettour-Janet, T. He, M. Perälä, P. Kronqvist, H. Joensuu, J. Ivaska, L-type calcium channels regulate filopodia stability and cancer cell invasion downstream of integrin signalling. *Nat. Commun.* **7**, 13297 (2016).

29. W. Hu, B. Wehrle-Haller, V. Vogel, Maturation of filopodia shaft adhesions is upregulated by local cycles of lamellipodia advancements and retractions. *PLOS ONE* **9**, e107097 (2014).

30. R. Kopan, M. X. G. Ilagan, The canonical Notch signaling pathway: Unfolding the activation mechanism. *Cell* **137**, 216–233 (2009).

31. C. M. Grochowski, K. M. Loomes, N. B. Spinner, Jagged1 (JAG1): Structure, expression, and disease associations. *Gene* **576**, 381–384 (2016).

32. T. Donnem, S. Andersen, K. Al-Shibli, S. Al-Saad, L.-T. Busund, R. M. Bremnes, Prognostic impact of Notch ligands and receptors in nonsmall cell lung cancer: Coexpression of Notch-1 and vascular endothelial growth factor-A predicts poor survival. *Cancer* **116**, 5676–5685 (2010).

33. Y. Li, M. A. Hibbs, A. L. Gard, N. A. Shylo, K. Yun, Genome-wide analysis of N1ICD/RBPJ targets in vivo reveals direct transcriptional regulation of Wnt, SHH, and hippo pathway effectors by Notch1. *Stem Cells* **30**, 741–752 (2012).

34. M. J. Oudin, O. Jonas, T. Kosciuk, L. C. Broye, B. C. Guido, J. Wyckoff, D. Riquelme, J. M. Lamar, S. B. Asokan, C. Whittaker, D. Ma, R. Langer, M. J. Cima, K. B. Wisinski, R. O. Hynes, D. A. Lauffenburger, P. J. Keely, J. E. Bear, F. B. Gertler, Tumor cell-driven extracellular matrix remodeling drives haptotaxis during metastatic progression. *Cancer Discov.* **6**, 516–531 (2016).

35. J. E. Schwarzbauer, D. W. DeSimone, Fibronectins, their fibrillogenesis, and in vivo functions. *Cold Spring Harb. Perspect. Biol.* **3**, a005041 (2011).

36. B. Erdogan, M. Ao, L. M. White, A. L. Means, B. M. Brewer, L. Yang, M. K. Washington, C. Shi, O. E. Franco, A. M. Weaver, S. W. Hayward, D. Li, D. J. Webb, Cancer-associated fibroblasts promote directional cancer cell migration by aligning fibronectin. *J. Cell Biol.* **216**, 3799–3816 (2017).

37. M. W. Conklin, J. C. Eickhoff, K. M. Riching, C. A. Pehlke, K. W. Eliceiri, P. P. Provenzano, A. Friedl, P. J. Keely, Aligned collagen is a prognostic signature for survival in human breast carcinoma. *Am. J. Pathol.* **178**, 1221–1232 (2011).

38. C. Bonnans, J. Chou, Z. Werb, Remodelling the extracellular matrix in development and disease. *Nat. Rev. Mol. Cell Biol.* **15**, 786–801 (2014).

39. R. Mayor, S. Etienne-Manneville, The front and rear of collective cell migration. *Nat. Rev. Mol. Cell Biol.* **17**, 97–109 (2016).

40. E. G. Heimsath Jr., Y.-I. Yim, M. Mustapha, J. A. Hammer, R. E. Cheney, Myosin-X knockout is semi-lethal and demonstrates that myosin-X functions in neural tube closure, pigmentation, hyaloid vasculature regression, and filopodia formation. *Sci. Rep.* **7**, 17354 (2017).

41. A. C. Bachg, M. Horsthemke, B. V. Skryabin, T. Klasen, N. Nagelmann, C. Faber, E. Woodham, L. M. Machesky, S. Bachg, R. Stange, H.-W. Jeong, R. H. Adams, M. Bähler, P. J. Hanley, Phenotypic analysis of Myo10 knockout (Myo10^{tm2/tm2}) mice lacking full-length (motorized) but not brain-specific headless myosin X. *Sci. Rep.* **9**, 597 (2019).

42. H. Tokuo, J. Bhawan, L. M. Coluccio, Myosin X is required for efficient melanoblast migration and melanoma initiation and metastasis. *Sci. Rep.* **8**, 10449 (2018).

43. A. Arjonen, R. Kaukonen, E. Mattila, P. Rouhi, G. Högnäs, H. Sihto, B. W. Miller, J. P. Morton, E. Bucher, P. Taimen, R. Virtakoivu, Y. Cao, O. J. Sansom, H. Joensuu, J. Ivaska, Mutant p53-associated myosin-X upregulation promotes breast cancer invasion and metastasis. *J. Clin. Invest.* **124**, 1069–1082 (2014).

44. R. Cao, J. Chen, X. Zhang, Y. Zhai, X. Qing, W. Xing, L. Zhang, Y. S. Malik, H. Yu, X. Zhu, Elevated expression of myosin X in tumours contributes to breast cancer aggressiveness and metastasis. *Br. J. Cancer* **111**, 539–550 (2014).

45. D. Li, M. Masiero, A. H. Banham, A. L. Harris, The Notch ligand JAGGED1 as a target for anti-tumor therapy. *Front. Oncol.* **4**, 254 (2014).

46. S. J. Bray, Notch signalling in context. *Nat. Rev. Mol. Cell Biol.* **17**, 722–735 (2016).

47. R. Pankov, E. Cukierman, B. Z. Katz, K. Matsumoto, D. C. Lin, S. Lin, C. Hahn, K. M. Yamada, Integrin dynamics and matrix assembly: Tensin-dependent translocation of alpha(5) beta(1) integrins promotes early fibronectin fibrillogenesis. *J. Cell Biol.* **148**, 1075–1090 (2000).

48. E. H. J. Danen, P. Sonneveld, C. Brakebusch, R. Fassler, A. Sonnenberg, The fibronectin-binding integrins α5β1 and αvβ3 differentially modulate RhoA-GTP loading, organization of cell matrix adhesions, and fibronectin fibrillogenesis. *J. Cell Biol.* **159**, 1071–1086 (2002).

49. G. Jacquemet, A. Stubb, R. Saup, M. Miihkinen, E. Kremneva, H. Hamidi, J. Ivaska, Filopodome mapping identifies p130Cas as a mechanosensitive regulator of filopodia stability. *Curr. Biol.* **29**, 202–216.e7 (2019).

50. Y. S. DeRose, K. M. Gligorich, G. Wang, A. Georgelas, P. Bowman, S. J. Courdy, A. L. Welm, B. E. Welm, Patient-derived models of human breast cancer: Protocols for in vitro and in vivo applications in tumor biology and translational medicine. *Curr. Protoc. Pharmacol.* **Chapter 14**, Unit14.23 (2013).

51. D. Montezuma, R. Azevedo, P. Lopes, R. Vieira, A. L. Cunha, R. Henrique, A panel of four immunohistochemical markers (CK7, CK20, TTF-1, and p63) allows accurate diagnosis of primary and metastatic lung carcinoma on biopsy specimens. *Virchows Arch.* **463**, 749–754 (2013).

52. A. N. Raines, S. Nagdas, M. L. Kerber, R. E. Cheney, Headless Myo10 is a negative regulator of full-length Myo10 and inhibits axon outgrowth in cortical neurons. *J. Biol. Chem.* **287**, 24873–24883 (2012).

53. Y. Tian, T. J. Morris, A. P. Webster, Z. Yang, S. Beck, A. Feber, A. E. Teschendorff, ChAMP: Updated methylation analysis pipeline for Illumina BeadChips. *Bioinformatics* **33**, 3982–3984 (2017).

54. B. G. Barwick, C. D. Scharer, A. P. R. Bally, J. M. Boss, Plasma cell differentiation is coupled to division-dependent DNA hypomethylation and gene regulation. *Nat. Immunol.* **17**, 1216–1225 (2016).

55. S. Anders, P. T. Pyl, W. Huber, HTSeq—A Python framework to work with high-throughput sequencing data. *Bioinformatics* **31**, 166–169 (2015).

56. S. Anders, W. Huber, Differential expression analysis for sequence count data. *Genome Biol.* **11**, R106 (2010).

57. M. Rupji, B. Dwivedi, J. Kowalski, NOJAH: NOt Just Another Heatmap for genome-wide cluster analysis. *PLOS ONE* **14**, e0204542 (2019).

58. J. Debnath, S. K. Muthuswamy, J. S. Brugge, Morphogenesis and oncogenesis of MCF-10A mammary epithelial acini grown in three-dimensional basement membrane cultures. *Methods* **30**, 256–268 (2003).

59. N. T. Seyfried, E. B. Dammer, V. Swarup, D. Nandakumar, D. M. Duong, L. Yin, Q. Deng, T. Nguyen, C. M. Hales, T. Wingo, J. Glass, M. Gearing, M. Thambisetty, J. C. Troncoso, D. H. Geschwind, J. J. Lah, A. I. Levey, A multi-network approach identifies protein-specific co-expression in asymptomatic and symptomatic Alzheimer's Disease. *Cell Syst.* **4**, 60–72.e4 (2017).

Citation: E. R. Summerbell, J. K. Mouw, J. S. K. Bell, C. M. Knippler, B. Pedro, J. L. Arnst, T. O. Khatib, R. Commander, B. G. Barwick, J. Konen, B. Dwivedi, S. Seby, J. Kowalski, P. M. Vertino, A. I. Marcus, Epigenetically heterogeneous tumor cells direct collective invasion through filopodia-driven fibronectin micropatterning. *Sci. Adv.* **6**, eaaz6197 (2020).